

# Optimization of random phase approximation calculations for improved energies of molecules, solids, and surfaces

Neung-Kyung Yu,<sup>†</sup> Johannes Voss,<sup>\*,†</sup> and Andrew J. Medford<sup>\*,†</sup>

<sup>†</sup> *School of Chemical & Biomolecular Engineering, Georgia Institute of Technology,  
Atlanta, Georgia 30332, USA*

<sup>‡</sup> *SUNCAT Center for Interface Science and Catalysis, SLAC National Accelerator  
Laboratory, Menlo Park, California 94025, USA*

E-mail: vossj@slac.stanford.edu; ajm@gatech.edu

## Abstract

We present an optimized random phase approximation method (optRPA26) that significantly improves upon conventional RPA. The method employs an empirically constructed hybrid functional to generate DFT orbitals to evaluate the RPA correlation energy, which is then scaled by a constant. Comprehensive benchmarks across molecules, bulk solids, and surface systems demonstrate that optRPA26 consistently achieves high accuracy, with mean absolute errors of 0.05 eV for W4-11 reaction energies, 0.07 eV for cohesive energies, 0.09 eV for metal oxide formation energies, 0.11–0.12 eV for adsorption of small molecules on metals, and 0.06 eV for adsorption on oxides. In addition, optRPA26 correctly captures phase stability in metal oxides and magnetic metals. The optRPA26 approach can be run using standard RPA implementations, highlighting its potential as a general-purpose reference method that can accurately capture covalent, ionic, and metallic, and van der Waals bonding in molecules, solids, and interfaces.

## 1 Introduction

Density functional theory (DFT) is the most widely used approach for quantum mechanical (QM) simulations in physics, materials science, and chemistry.<sup>1</sup> Many problems in applied sciences require computing properties of systems with  $\sim$ 100 atoms or more, often with periodic or mixed boundary conditions. DFT is capable of performing these simulations within a practical time frame due to its relatively low computational cost and the wide availability of efficient implementations. However, the lack of a universally accurate exchange-correlation (xc) functional leads to errors that can greatly exceed the “chemical accuracy” (1 kcal mol<sup>−1</sup> or 0.043 eV) needed for quantitative predictions of reaction rates.<sup>2</sup> For transition metal systems, the uncertainty is even greater from both experimental and theoretical points of view, so the chemical precision of the transition metals (3 kcal mol<sup>−1</sup> or 0.130 eV) has been defined more loosely.<sup>3–5</sup> Although numerous specialized functionals exist, the lack of systematic im-

provement in functionals makes it difficult to determine a priori which approximation will be most accurate for a particular chemical system. The development of an xc functional that achieves chemical accuracy across all types of systems—including atoms, molecules, liquids, ionic solids, metals, and interfaces—is a grand challenge in the field of computational chemistry.<sup>6,7</sup> The problem is particularly acute in surface science in catalysis, where there is currently no method capable of achieving chemical accuracy for adsorption at metal surfaces.<sup>8</sup>

Wavefunction methods offer a more accurate alternative to DFT. However, their high computational cost and limited availability of periodic implementations make them impractical for many problems in materials science and solid-state physics. Nevertheless, two wavefunction approaches have become increasingly efficient and have been applied to solid-state problems with periodic boundary conditions. The first is coupled cluster with singles, doubles, and partial triples (CCSD(T)), widely regarded as the gold standard for chemical calculations, achieving chemical accuracy in most systems where it can be applied.<sup>9,10</sup> Although CCSD(T) is computationally very expensive, with formal  $\mathcal{O}(N^7)$  scaling,<sup>9,10</sup> more efficient approaches have been developed.<sup>11</sup> Specifically, recent progress in local approximations to CCSD(T) led to the development of variants such as PNO-CCSD(T),<sup>12</sup> and DLPNO-CCSD(T),<sup>13</sup> and LNO-CCSD(T).<sup>14–16</sup> In practice, CCSD(T) is primarily applied for gas molecules since most implementations do not support periodic boundary conditions. However, periodic CCSD(T) implementations have recently become available.<sup>17</sup> Several groups have successfully applied local CCSD(T) methods (both periodic and non-periodic) to calculate highly accurate adsorption energies on oxide surfaces.<sup>8,18–21</sup> Despite this progress, the implementation of partial triples (T) remains problematic for metallic systems due to energy divergence, also known as the infrared catastrophe.<sup>17,22</sup> Only very recently, a modified approximation to the triples (cT) has been proposed to address this limitation.<sup>23–25</sup>

In addition, quantum Monte Carlo (QMC) methods, such as diffusion Monte Carlo (DMC), have been applied even more widely to problems in solid-state physics and sur-

face science.<sup>26–28</sup> In principle, DMC is an exact method, but its accuracy is typically limited by practical factors such as the number of moves for statistical sampling, time step size, specialized pseudopotentials, and slow convergence of Brillouin zone sampling via supercell extrapolation, as well as the fixed-node approximation.<sup>26,27,29,30</sup> Although generally much more accurate than DFT, statistical error bars on practical quantities such as formation energies and adsorption energies often exceed chemical precision.<sup>28,31,32</sup> Due to the lack of highly accurate and practical computational methods for surfaces, there are only a few well-established reference datasets, such as the CE39<sup>33</sup> or ADS41 dataset<sup>34</sup> of experimental and DFT adsorption energies on simple metal surfaces.

Another strategy to improve upon DFT methods is the use of embedding schemes that combine low-level and high-level QM methods. The high-level method is typically applied to small clusters, whereas the low-level method is used to describe larger systems, such as periodic models. Embedding approaches have been applied to describe adsorption on oxide surfaces using MP2 or CCSD(T) as the high-level method<sup>18,19,21,35–37</sup> and on metal surfaces using hybrid functionals, RPA, or wavefunction theories as the high-level method.<sup>38–42</sup> In particular, the *PBE+D3/M06* approach is an embedding scheme that combines cluster (at hybrid M06 level) and periodic models (at PBE+D3 level). This approach has been reported as one of the most accurate methods for adsorption energies on metals and is therefore used as a comparison in this benchmarking study. Despite the potential for high accuracy in embedding methods, they generally require specialized software and expertise, and are not widely used in the computational materials science community.

Returning to standard DFT, the concept of Jacob's ladder of density functional approximations describes the physical hierarchy of density-based quantum chemical methods into five levels.<sup>43</sup> Different levels of DFT methods are positioned on each rung, starting with the local density approximation (LDA) on the first rung, followed by the generalized gradient approximation (GGA), meta-GGA, and hybrid functionals. Unlike those on the lower rungs, the methods on the fifth rung consider unoccupied orbitals for *ab initio* calculation of corre-

lation energy, with the random phase approximation (RPA) located at this level. RPA correlation energies are computed with help of the adiabatic connection fluctuation-dissipation theorem (ACFDT), where the interacting density response function is approximated at the RPA level. The ACFDT was established over 40 years ago,<sup>44</sup> but ACFDT-RPA correlation energies have not become a standard choice. While RPA is generally applicable to solids, it remains computationally expensive and exhibits limited accuracy, particularly for molecular systems, despite its physical soundness.<sup>45,46</sup>

There have been continued efforts to improve the accuracy of RPA. One strategy involves correcting the relatively less accurate short-range RPA correlation using the short-range LDA or GGA correlation. This concept underlies the RPA+<sup>47</sup> and the generalized RPA+,<sup>48</sup> which have been applied to atomic or molecular systems. An alternative approach introduces a second-order screened exchange (SOSEX) term to the RPA energy, leading to the RPA+SOSEX method.<sup>49</sup> Similarly, singles excitation (SE) and renormalized singles excitation (rSE) contributions have been proposed, resulting in RPA+SE, RPA+rSE, and RPA+SOSEX+rSE.<sup>50,51</sup> Although these corrections improve the accuracy of RPA, their overall performance remains limited and often unbalanced.<sup>50,52</sup> Other beyond-RPA methods, based on time-dependent DFT, include the renormalized adiabatic local density approximation (rALDA) and the renormalized adiabatic Perdew–Burke–Ernzerhof (rAPBE) xc kernels.<sup>53</sup> These approaches show even higher accuracy across different classes of systems.<sup>54</sup> Despite the promise of these approaches, most are not widely available in standard electronic structure packages, and thus require specialized expertise or software, limiting their application in practice.

In contrast, the approach introduced in this work focuses on optimizing the standard RPA calculation, often referred to as direct RPA,<sup>55</sup> to achieve substantially higher accuracy at the cost of generating hybrid-level wavefunctions, while leveraging widely implemented RPA algorithms. In standard RPA, the total RPA energy is typically evaluated on PBE orbitals (referred to as RPA@PBE), but RPA calculations using a hybrid PBE0 functional

(RPA@PBE0) have also been reported.<sup>39,56</sup> In a prior study, we used a global PBE hybrid with 50% exact exchange (EXX) to incorporate non-local interactions and then scaled the RPA correlation energy,<sup>57</sup> which we refer to here as optRPA24. This approach yielded accurate results for molecular atomization and formation energies, but suffered from energy convergence issues in the adsorption energies on metallic surfaces. In addition, the hybrid functional used for the wavefunctions did not yield the correct magnetic properties for bulk magnetic metals. Here, we use a long-range corrected (LC) custom hybrid functional that includes 25% EXX only in the long range to construct DFT orbitals. The RPA correlation energy is then scaled by a constant, which is fitted using the W4-11 dataset of highly accurate molecular atomization energies. Finally, short-range PBE correlation is applied when evaluating the non-RPA correlation part of total energy, which reduces the optimal scaling constant to  $\sim 1$  and improves energy convergence. The approach of scaling the RPA correlation energy has been reported in LC double-hybrid frameworks, where the total energy includes long-range EXX and long-range RPA correlation.<sup>58,59</sup> Our optimized RPA approach, which we refer to as optRPA26, can be run using a standard VASP installation (compiled with the Libxc library<sup>60</sup>) without modification to the source code, making it a practical alternative to more specialized approaches. Here, we present the details of the formulation and benchmark it against a diverse dataset of molecules, bulk solids, and surfaces, demonstrating that optRPA26 can serve as a highly accurate reference method for general systems in computational chemistry and catalysis.

## 2 Methods

Details of the benchmark datasets and electronic structure calculations are summarized here. Additional details are provided in the SI.

## 2.1 Benchmark Datasets

The following benchmark datasets were used as ground-truth reference values in this work. Additional details of data curation and computational protocols are provided in the Details of Benchmark Datasets section of the SI.

- Molecular atomization energies (W4-11):<sup>61</sup>
  - 140 atomization energies of small molecules and radicals, calculated using highly accurate W4 theory.<sup>62</sup>
  - We considered 124 molecules with less multireference character (TAE\_nonMR124 subset<sup>61</sup>), which should be more relevant for catalysis. A list of excluded molecules can be found in Ref. 63.
- Molecular reaction energies (W4-11-RE):<sup>64</sup>
  - 11,247 reaction energies derived from the W4-11 dataset.
  - We selected only reactions involving molecules in TAE\_nonMR124, resulting in 8,868 reactions.
- Molecular barrier heights (BH76):<sup>65–67</sup>
  - 76 forward and reverse barrier heights for hydrogen transfer, heavy-atom transfer, nucleophilic substitution, unimolecular, and association reactions.
- Molecular reaction energies (BH76RC):<sup>67</sup>
  - 30 reaction energies derived from the BH76 dataset.
- Reactions of organometallic transition metal (TM) complexes (MOBH29):<sup>68–71</sup>
  - A revised version of MOBH35.<sup>68</sup>
  - 29 forward and 29 backward barrier heights, as well as 29 reaction energies.

- Non-covalent interaction energies (S19):
  - We selected 19 interaction energies from the S66 dataset.<sup>72</sup>
- Bulk solid datasets:
  - 24 lattice constants, 24 bulk moduli, and 24 atomization energies of non-oxides.<sup>73,74</sup>
  - 23 oxide formation energies.<sup>75,76</sup>
  - Magnetic moments of magnetic solids (Fe, Co, and Ni).<sup>77</sup>
  - Relative stability of bulk phases of Co (hcp, fcc, and bcc phases), MoO<sub>3</sub> ( $\alpha$  and  $\beta$  phases), and TiO<sub>2</sub> (rutile and anatase phases).
- Surface datasets:
  - 27 experimental adsorption energies on transition metal surfaces derived from ADS41.<sup>33,34,78</sup>
  - 7 surface reaction energies on oxide surfaces (5 CCSD(T)-level calculation values<sup>8,20</sup> and 2 experimental values<sup>21</sup>).
  - Surface energies of four transition metal surfaces with (111) facet.<sup>79</sup>

## 2.2 Computational Details

All periodic calculations were performed using the Vienna Ab initio Simulation Package (VASP) version 6.3.2, employing projector-augmented wave (PAW) pseudopotentials.<sup>80–83</sup> GW-type PAW pseudopotentials (version 54) were used throughout. Specifically, the pseudopotentials recommended by VASP<sup>84</sup> were employed, except for C, N, O, and F, for which “GW\_new” pseudopotentials were used. Another exception was for metal slab calculations, where GW pseudopotentials with the fewest valence electrons were selected. The GW pseudopotentials used for the metal slabs do not include semi-core s and p states in Ni, Cu, Rh, Pd, and Pt, while those for Ru and Ir include them.

Spin polarization was considered only for magnetic materials, including Fe, Ni, and Co-containing systems and alkali-metal superoxides ( $\text{NaO}_2$ ,  $\text{KO}_2$ ,  $\text{RbO}_2$ , and  $\text{CsO}_2$ ). The fast Fourier transform (FFT) grids for GGA (PREC) and exact exchange (PRECFOCK) were set to “Accurate” and “Normal”, respectively, with the exception of calculations for non-oxide bulk systems (see Section S1.2.2 of the SI).

For DFT calculations, the following dispersion-corrected DFT functionals were used: PBE+D3 (GGA),<sup>85,86</sup> r2SCAN+rVV10 (meta-GGA),<sup>87–89</sup> and HSE06+D3 (hybrid).<sup>86,90</sup> All other calculation parameters were identical to those used for RPA calculations, unless otherwise specified. Structural relaxations were performed using PBE+D3, and the same structures were used for single-point calculations with all functionals.

For RPA calculations, a cubic-scaling algorithm was used<sup>91</sup> with a frequency integration grid containing 24 points. We used an empirically constructed custom hybrid functional, LC-srPBEx25, to generate DFT orbitals for evaluating the RPA correlation energy. This functional uses a long-range corrected hybrid scheme with a range separation parameter ( $\mu$ ) of  $3.0\text{\AA}^{-1}$  and 25% exact exchange. The GGA xc component was described using the short-range PBE (srPBE) functional<sup>92–94</sup> with the default range separation parameter of  $0.94\text{\AA}^{-1}$  (0.5 Bohr<sup>-1</sup>) for both exchange ( $\mu$ ) and correlation ( $\mu_c$ ) via the Libxc library (version 7.0.0).<sup>60</sup> The LC-srPBEx25 functional includes 25% long-range (lr) exact exchange, 75% srPBE exchange, and 500% srPBE correlation (see Section 4.1 in the Discussion), as defined below. This empirically constructed functional is used solely to generate Kohn–Sham orbitals, which have been found to serve as suitable inputs for RPA energy evaluation. Its exchange-correlation energy is calculated as:

$$E_{\text{xc, LC-srPBEx25}} = (0.25 \cdot E_{\text{x,EXX}}^{\text{lr},\mu=3.0\text{\AA}^{-1}} + 0.75 \cdot E_{\text{x,srPBE}}^{\text{sr},\mu=0.94\text{\AA}^{-1}}) + 5.00 \cdot E_{\text{c,srPBE}}^{\text{sr},\mu_c=0.94\text{\AA}^{-1}} \quad (1)$$

where  $E_{\text{x,EXX}}^{\text{lr},\mu=3.0\text{\AA}^{-1}}$  is long-range exact exchange,  $E_{\text{x,srPBE}}^{\text{sr},\mu=0.94\text{\AA}^{-1}}$  is short-range PBE exchange, and  $E_{\text{c,srPBE}}^{\text{sr},\mu_c=0.94\text{\AA}^{-1}}$  is short-range PBE correlation.

The total energy in the standard RPA calculation is defined as

$$E_{\text{total}}^{\text{RPA}} = E_{\text{HXX}} + E_{c,\text{RPA}} \quad (2)$$

where  $E_{\text{HXX}}$  is HF energy (HF@PBE) and  $E_{c,\text{RPA}}$  is the RPA correlation energy (RPA<sub>c</sub>@PBE), both evaluated using PBE orbitals. In optRPA24,<sup>57</sup> the previous version of optRPA26, the total energy is defined as

$$E_{\text{total}}^{\text{optRPA24}} = E_{\text{HXX}} + r_c \cdot E_{c,\text{RPA}} \quad (3)$$

where  $E_{\text{HXX}}$  (HF@PBEx50) and  $E_{c,\text{RPA}}$  (RPA<sub>c</sub>@PBEx50) are evaluated using PBEx50 (a PBE global hybrid with 50% EXX) orbitals, and  $r_c$  ( $=1.180$ ) is a scaling constant for  $E_{c,\text{RPA}}$ . In optRPA26, the total energy is defined as

$$E_{\text{total}}^{\text{optRPA26}} = E_{\text{optHXX}} + r_c \cdot E_{c,\text{RPA}} \quad (4)$$

where  $E_{\text{optHXX}}$  is the modified HXX energy that includes a non-RPA correlation contribution of the total energy. Both  $E_{\text{optHXX}}$  (optHXX@LC-srPBEx25) and  $E_{c,\text{RPA}}$  (RPA<sub>c</sub>@LC-srPBEx25) are evaluated using the same LC-srPBEx25 orbitals. Each term in Eq. (4) is obtained from a separate single-point calculation. The xc part of optHXX consists of 100% full-range EXX ( $E_{\text{x,EXX}}$ ) and 20% srPBE correlation ( $E_{\text{c,srPBE}}^{\text{sr},\mu_c=1.89\text{\AA}^{-1}}$ ) with a range separation parameter for DFT correlation of  $1.89\text{\AA}^{-1}$  ( $=1.0\text{ Bohr}^{-1}$ ):

$$E_{\text{xc,optHXX}} = E_{\text{x,EXX}} + 0.20 \cdot E_{\text{c,srPBE}}^{\mu_c=1.89\text{\AA}^{-1}} \quad (5)$$

The srPBE correlation was introduced to reduce  $r_c$  for optRPA26 (from 1.114 to 1.02), which improves energy convergence (see Section 4.3 in the Discussion). We did not include a correction to the non-RPA correlation part for partial occupancies,<sup>73</sup> as it did not help energy convergence (Fig. S9).

For RPA calculations, we applied a plane-wave energy cutoff ( $E_{\text{cutoff}}$ ) correction term

$\Delta_{\text{cutoff}}$  for all calculations, except for molecular datasets and non-oxide bulk solids, for which a sufficiently large  $E_{\text{cutoff}}$  of 500–600 eV can be used without this correction. The correction is defined as:

$$\Delta_{\text{cutoff}} = \Delta E_{\text{low-k, high-E}} - \Delta E_{\text{low-k, low-E}} \quad (6)$$

The  $\Delta_{\text{cutoff}}$  is the difference in the calculated energy change  $\Delta E$  (e.g., reaction energy) obtained using low and high  $E_{\text{cutoff}}$  (low-E and high-E, respectively) with a coarse k-point grid (low-k). The correction is added to  $\Delta E_{\text{high-k, low-E}}$  to obtain an accurate energy  $\Delta E_{\text{high-k, high-E}}$  at a dense k-point grid (high-k),

$$\Delta E_{\text{high-k, high-E}} \approx \Delta E_{\text{high-k, low-E}} + \Delta_{\text{cutoff}} \quad (7)$$

The  $\Delta_{\text{cutoff}}$  has been reported to be largely independent of k-point meshes and can recover  $\Delta E_{\text{high-k, high-E}}$  almost perfectly<sup>95–98</sup> (Fig. S5).

For RPA calculations of molecules involved in bulk solid and surface datasets, we extrapolated  $E_{\text{optHXX}}$  and  $E_{\text{c,RPA}}$  with respect to cell volumes ( $V$ ) to the limit of infinitely dilute gas, using the form  $E = E_{\infty} + \alpha V^{-1} + \beta V^{-2}$ , where  $E_{\infty}$  is the energy of a molecule in an infinitely large cell<sup>99</sup> (Fig. S13 and S14).  $E_{\infty}$  is correlated with the total number of electrons ( $N$ ) and the number of valence electrons ( $N_{\text{v}}$ ) in gas species (Fig. S15). Therefore, the volume dependence of molecular energies should be considered for gas species with a large number of electrons, such as I and  $\text{CH}_3\text{I}$ , to obtain accurate adsorption energies. For DFT calculations, a large cubic cell (20 Å) was used without applying the extrapolation scheme. The energy difference between HSE06 results using 15 Å and 20 Å cells was less than 0.001 eV. The Coulomb divergence of exact exchange was corrected using the probe-charge method<sup>100,101</sup> (`HFRCUT=0` in VASP, which is the default), except for bulk calculations used for surface energy evaluations (see Section S1.2.3 of the SI).

More computational details can be found in Sections S1.2 and S1.5 of the SI.

## 2.3 Adsorption energy definitions

Evaluating the thermochemistry of adsorbates is non-trivial, since both gas-phase and surface properties are involved, and it is not always straightforward to establish whether error occurs due to the gas-phase reference state or the adsorbed state. Several definitions of adsorption energies exist in the literature,<sup>102</sup> and here we adopt the following three definitions:

$$E_{\text{ads}} = E_{\text{slab+ads}} - E_{\text{slab}} - E_{\text{ads(g)}} \quad (8)$$

$$E_{\text{diss}} = \sum_i \nu_i (E_{\text{slab+ads},i} - E_{\text{slab}}) - E_{\text{mol}} \quad (9)$$

$$E_{\text{ads,LS}} = E_{\text{slab+ads}} - E_{\text{slab}} - \sum_k n_k \mu_{\text{LS},k} \quad (10)$$

where  $E_{\text{slab+ads}}$  is the combined slab and adsorbate system,  $E_{\text{slab}}$  is the bare slab,  $E_{\text{ads(g)}}$  is the adsorbate directly in the gas-phase,  $E_{\text{mol}}$  is a gas-phase molecule that dissociates into  $E_{\text{slab+ads},i}$ ,  $\nu_i$  denotes the stoichiometric coefficient of adsorbate  $i$  in dissociative adsorption,  $n_k$  is the number of elemental species  $k$  in the adsorbate, and  $\mu_{\text{LS},k}$  is a chemical potential of an elemental species that is obtained through least-squares regression.<sup>102</sup>

The first definition is the most straightforward, as it represents non-dissociative adsorption. However, significant errors can be introduced because the gas-phase analogues of the adsorbates may be unstable open-shell radicals with complex electronic structure not well captured by DFT (e.g. bare O atoms, CH fragments, etc.). We obtained the reference values for the first definition by applying the same approach to ADS41 as in Ref. 78, but using different molecular energies obtained from the AtCT database<sup>103</sup> and zero point energies (ZPE) from literature.<sup>104–107</sup> For adsorption of CH and CH<sub>3</sub>, ZPE-corrected experimental values were used.<sup>108,109</sup>

The second definition minimizes the use of open-shell reference states by treating the adsorption event as a dissociation of a stable gas-phase species, and normalizing the energy to be per mole of adsorbate ( $E_{\text{diss}}(H) = \Delta E/2$ , considering H<sub>2</sub>→2H). One advantage of

referencing  $E_{\text{ads}}$  to molecules is that spin-orbit coupling (SOC) effects are diminished. For example, the I atom has a spin-orbit stabilization energy of -0.31 eV, whereas the value for the  $\text{I}_2$  molecule is -0.09 eV.<sup>110</sup> Given that SOC effects are not accounted for in the methods investigated here, we applied SOC correction terms to all calculated energies involving I-containing species in both adsorption definitions. Still, this approach does not guarantee reduced gas-phase error because some molecules are difficult to describe accurately using DFT, such as  $\text{O}_2$  (whose triplet state is the ground state). In cases where the adsorbate does not dissociate (e.g., CO, NO,  $\text{CH}_4$ , etc.) the two definitions are identical. For other species, conversion between the definitions requires knowledge of the gas-phase molecular energies. For the  $PBE+D3/M06$  method, only the first definition ( $E_{\text{ads}}$ ) was reported in the original paper, and gas-phase energies were not reported. Therefore, we calculated molecular energies at the same level of theory, using ORCA version 5.0.4<sup>111</sup> and the def2-QZVPP basis set to convert between the two:<sup>112</sup>

$$E_{\text{gas}}^{\text{PBE+D3/M06}} = E_{\text{gas}}^{\text{PBE+D3, periodic}} + (E_{\text{gas}}^{\text{M06, cluster}} - E_{\text{gas}}^{\text{PBE+D3, cluster}})$$

where  $E_{\text{gas}}$  includes both  $E_{\text{ads(g)}}$  and  $E_{\text{mol}}$ ,  $E_{\text{gas}}^{\text{PBE+D3, periodic}}$  is molecular energies at PBE+D3 level under periodic boundary conditions (calculated using VASP), and  $E_{\text{gas}}^{\text{M06, cluster}}$  and  $E_{\text{gas}}^{\text{PBE+D3, cluster}}$  are the corresponding energies computed in a cluster model at M06 and PBE+D3 levels (calculated using ORCA).

The third definition of adsorption energies,  $E_{\text{ads,LS}}$ , avoids issues of reference state error by obtaining reference chemical potentials using least-squares (LS) regression. The  $\mu_{\text{LS},i}$  are determined by minimizing the squared magnitude of the adsorption energy  $E_i$ :<sup>102</sup>

$$\boldsymbol{\mu}_{\text{LS}} = \arg \min_{\boldsymbol{\mu}} \sum_{i=1} \left( E_i - \sum_{k=1} n_{i,k} \mu_k \right)^2 \quad (11)$$

where  $\boldsymbol{\mu}$  is a  $(k \times 1)$  vector of elemental chemical potentials  $\mu_k$ ,  $E_i$  is QM energy of species  $i$ , and  $n_{i,k}$  is the number of element  $k$  in species  $i$  (and includes only elements in the adsorbates).

In this case,  $E_i$  corresponds to  $(E_{\text{slab+ads}} - E_{\text{slab}})$  for computed adsorption energies and  $(E_{\text{ads}} + \Delta E_{\text{f, ads(g)}}$ ) for experimental adsorption energies, where  $\Delta E_{\text{f, ads(g)}}$  is the formation energy of gas-phase adsorbate (i.e., the formation enthalpy at 0 K with ZPE contributions removed) obtained from AtCT. This minimization can be efficiently solved using linear algebra:

$$\boldsymbol{\mu}_{\text{LS}} = (\mathbf{N}^T \mathbf{N})^{-1} \mathbf{N}^T \mathbf{E} \quad (12)$$

$$\boldsymbol{\mu}_{\text{LS}} = \begin{pmatrix} \mu_{\text{LS},1} \\ \mu_{\text{LS},2} \\ \vdots \\ \mu_{\text{LS},k} \end{pmatrix}, \quad \mathbf{N} = \begin{pmatrix} n_{1,1} & n_{1,2} & \cdots & n_{1,k} \\ n_{2,1} & n_{2,2} & \cdots & n_{2,k} \\ \vdots & \vdots & \ddots & \vdots \\ n_{i,1} & n_{i,2} & \cdots & n_{i,k} \end{pmatrix}, \quad \mathbf{E} = \begin{pmatrix} E_1 \\ E_2 \\ \vdots \\ E_i \end{pmatrix} \quad (13)$$

where  $\mathbf{N}$  is a stoichiometry matrix ( $i \times k$ ) with elements  $n_{i,k}$  and  $\mathbf{E}$  is an ( $i \times 1$ ) vector of QM energies  $E_i$  of each species. This approach eliminates the need for any gas-phase reference, and can be shown to minimize the squared errors between energies from different sources.<sup>102</sup> However, it introduces one degree of freedom for each element involved and can thus underestimate the error for datasets with few examples of an element (e.g. iodine). It also removes all systematic error by construction, so that systematic over- or under-binding of molecules will not show up in this definition since the error will be pushed into the reference states. Finally, the specific values of  $\mu_{\text{LS},i}$  are also dependent on the dataset used, and it is thus not a physically meaningful quantity in general. Nonetheless, it provides a useful perspective on the adsorption error since it directly probes the error that arises from the surface and adsorbate and establishes a lower bound on a practical adsorption energy error.

### 3 Results

The performance of the proposed optRPA26 method was benchmarked against the various datasets introduced earlier. For comparison, we also evaluated representative DFT functionals (PBE+D3, r2SCAN+rVV10, and HSE06+D3) and included data from higher-level methods from the literature where available. We report energy errors using mean absolute deviation (MAD), root mean square deviation (RMSD), and maximum absolute deviation. For lattice constants and bulk moduli, mean absolute percentage deviation (MAPD), root mean square percentage deviation (RMSPD), and maximum absolute percentage deviation are reported.

#### 3.1 Molecular Datasets

Benchmarking results for different molecular datasets are presented in Fig. 1. For W4-11 (atomization energy), PBE+D3 showed a significantly higher RMSD (0.81 eV) than other DFT functionals, but performed comparably for W4-11-RE (reaction energy) with an RMSD of 0.27 eV, suggesting substantial error cancellation. Similar behavior was observed for RPA, with RMSDs of 0.86 eV (W4-11) and 0.20 eV (W4-11-RE). The largest errors of RPA in W4-11-RE were associated with the HS molecule, and the comparable performance of RPA and PBE+D3 on gas-phase properties is consistent with prior benchmarking for ethane dehydrogenation.<sup>113</sup> For BH76 (barrier height), the accuracy of DFT functionals followed their hierarchy on Jacob’s ladder, with RMSDs of 0.46 eV (PBE+D3), 0.35 eV (r2SCAN+rVV10), and 0.22 eV (HSE06+D3). Similar trends were observed for BH76RC (reaction energy) and MOBH29 (barrier height and reaction energy of TM complex), albeit with smaller differences among the functionals. DFT methods showed mutually similar accuracy for S19 (non-covalent binding energy), with RMSDs of 0.03–0.04 eV. The optRPA26 method consistently outperformed all tested methods, yielding RMSDs of 0.17 eV (W4-11), 0.06 eV (W4-11-RE), 0.09 eV (BH76), 0.10 eV (BH76RC), 0.09 eV (MOBH29), and 0.01

eV (S19). Notably, the maximum error for optRPA26 on W4-11-RE is 0.27 eV, which is substantially lower than all other methods ( $\sim 1$  eV), indicating that the approach will be generally reliable for reaction energies, with similar trends observed for barrier heights.

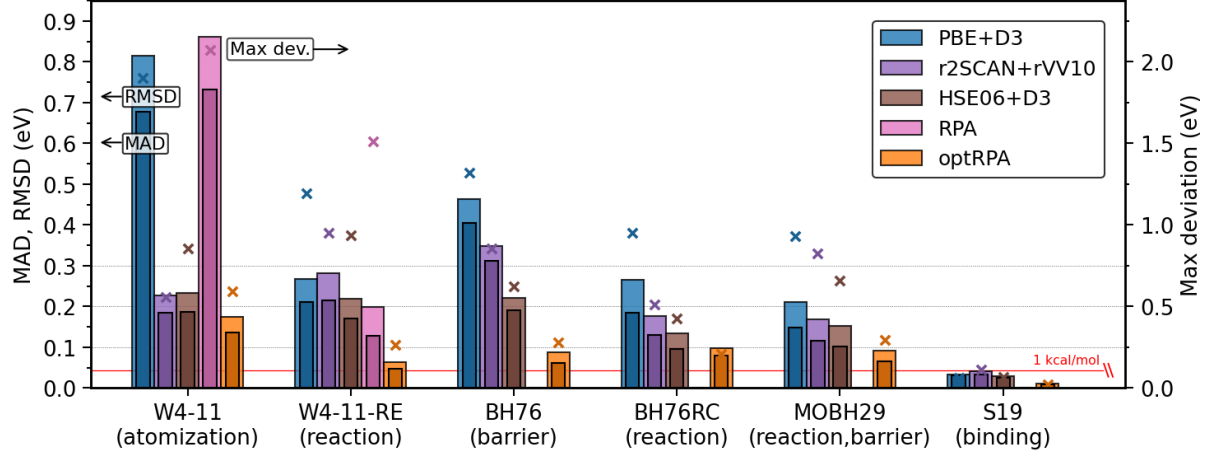


Figure 1: Absolute deviations from reference values for each molecular dataset. Datasets include W4-11 ( $n=124^*$ ),<sup>61</sup> W4-11-RE ( $n=8,868^*$ ),<sup>64</sup> BH76 ( $n=76$ ),<sup>65-67</sup> BH76RC ( $n=30$ ),<sup>67</sup> MOBH29 ( $n=87$ ),<sup>68-71</sup> and S19 ( $n=19$ ).<sup>72</sup> Bars represent MAD (dark color) and RMSD (light color), and  $\times$  symbols indicate maximum deviations. A horizontal red line denotes the chemical accuracy of 1 kcal/mol. \*W4-11 and W4-11-RE contain only the molecules listed in TAE\_nonMR124.

## 3.2 Bulk Solid Datasets

### 3.2.1 Lattice constant and bulk modulus

The calculated bulk lattice constants and bulk moduli for non-oxide solids are presented in Fig. 2. In both lattice constants and bulk moduli, optRPA26 showed good accuracy with RMSPD of 0.37% and 5.16%, respectively, comparable to the best-performing methods, RPA (0.48% and 4.64%) and rALDA (0.75% and 5.39%). The accuracy of rAPBE is difficult to assess because only four data points are available (for lattice constants only). PBE+D3 delivered good performance for lattice constants (RMSPD of 0.85%) and bulk moduli (8.83%), but the D3 correction was necessary because, without it, RMSPD increased to 1.64% and 14.51%, respectively. Among DFT methods, r2SCAN+rVV10 produced the most accurate results, outperforming HSE06+D3.

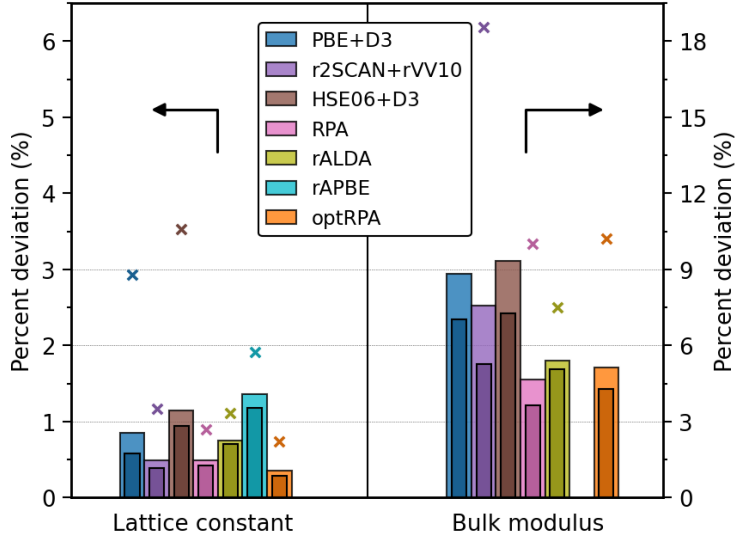


Figure 2: Absolute percentage deviations from ZPE-corrected experimental values for lattice constants<sup>73</sup> and bulk moduli<sup>73,74</sup> for 24 (non-oxide) bulk solids. RPA (n=24),<sup>73</sup> rALDA (n=10),<sup>114</sup> and rAPBE (n=4)<sup>53</sup> values are taken from the literature. Bars represent MAPD (dark color) and RMSPD (light color), and  $\times$  symbols indicate maximum percentage deviations.

### 3.2.2 Atomization energy of non-oxide and oxide formation energy

The calculated atomization energies of non-oxides and oxide formation energies are presented in Fig. 3. optRPA26 performed well for both datasets with RMSDs of 0.10 eV (atomization energy) and 0.12 eV (oxide formation energy), comparable to the best-performing methods for each dataset, which are rAPBE (0.07 eV) for atomization energy and r2SCAN+rVV10 (0.13 eV) for oxide formation energy, respectively. As observed earlier for lattice constants and bulk moduli, r2SCAN+rVV10 again showed the highest accuracy for the bulk properties among DFT methods. The reference values for oxide formation are not ZPE-corrected, but this effect is reported to change the MAD of the current dataset by, at most, 0.01 eV.<sup>75</sup>

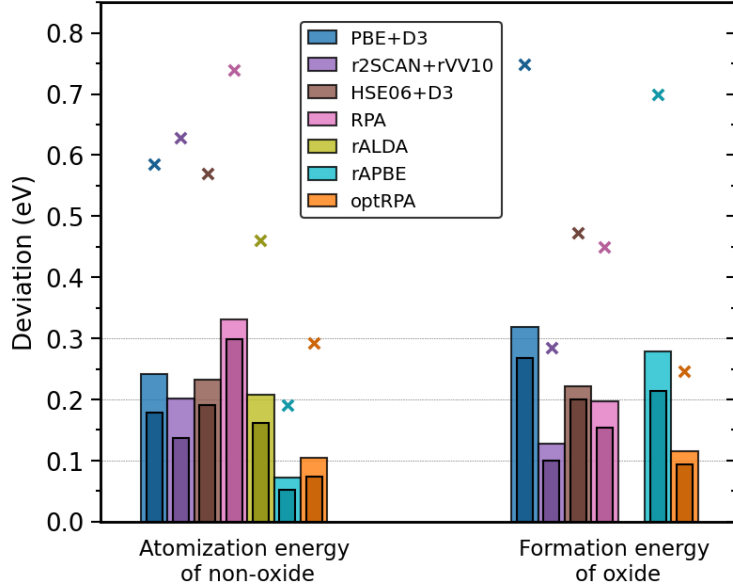


Figure 3: Absolute deviations from (ZPE-corrected) experimental atomization energies (eV per formula unit) of 24 non-oxides<sup>73</sup> and (non-ZPE-corrected) formation energies (eV per oxygen) of 23 oxides.<sup>75,76</sup> For atomization energies, RPA values (n=24) are from Ref. 73, and rALDA (n=19) and rAPBE (n=19) are from Ref. 53. For oxide formation energies, RPA values (n=22) are from Ref. 75, and rAPBE values (n=21) are from Ref. 95. Bars represent MAD (dark color) and RMSD (light color), and  $\times$  symbols indicate maximum deviations.

### 3.2.3 Magnetic moments of metals

We evaluated the magnetic moments of elemental ferromagnets (Fe, Co, and Ni) to assess the performance of different functionals in capturing the correct spin polarization, as shown in Table 1. PBE values show good agreement with experimental values, while HSE06 (and hybrid functionals in general) tends to significantly overestimate the spin magnetic moments, with a similar trend observed for the meta-GGA r2SCAN. In contrast, LC-srPBEx25 reproduces the correct experimental magnetic moments, similar to PBE. We note that this property depends only on the LC-srPBEx25 method, not optRPA26 itself, but it confirms that the orbitals used in optRPA26 for spin-polarized metals have qualitatively accurate magnetic properties.

Table 1: Spin magnetic moment ( $\mu_B$ ) of magnetic bulk solids calculated with different functionals. Values outside parentheses correspond to PBE+D3-optimized structures, while values in parentheses correspond to structures with experimental lattice constants.

Method	Fe	Co	Ni
PBE+D3	2.115 (2.191)	1.586 (1.633)	0.654 (0.649)
r2SCAN+rVV10	2.544 (2.657)	1.734 (1.763)	0.740 (0.775)
HSE06+D3	2.748 (2.823)	1.841 (1.917)	0.873 (0.888)
LC-srPBEx25	2.057 (2.144)	1.586 (1.635)	0.625 (0.652)
Experiment <sup>77</sup>	2.13	1.52	0.57

### 3.2.4 Relative stability of bulk solids

We evaluated the relative stability of bulk polymorphs for Co,  $\text{MoO}_3$ , and  $\text{TiO}_2$ , where standard DFT often fails to predict the correct ground-state phase.<sup>115–117</sup> optRPA26 correctly predicts the most stable phases for all systems considered, albeit by very small energy differences, as shown in Table 2. We note that it is possible that the experimentally observed ground-state phase may not have the lowest energy at 0 K, as thermal effects may play a role.<sup>118</sup>

Table 2: Relative energy (eV) of Co,  $\text{MoO}_3$ , and  $\text{TiO}_2$  bulks in different phases. The smallest value (bold) corresponds to the most stable phase within each formula. Values outside parentheses correspond to PBE+D3-optimized structures, while values in parentheses correspond to structures with experimental lattice constants.<sup>119</sup>

Method	Co			$\text{MoO}_3$			$\text{TiO}_2$	
	hcp Co	fcc Co	bcc Co	$\alpha\text{-MoO}_3$	$\beta\text{-MoO}_3$	rutile	anatase	
PBE+D3	<b>0</b>	0.022	0.096	0	<b>-0.075</b>	0	<b>-0.014</b>	
r2SCAN+rVV10	0	-0.024	<b>-0.037</b>	0	<b>-0.030</b>	0	<b>-0.002</b>	
HSE06+D3	0	-0.225	<b>-0.267</b>	0	<b>-0.077</b>	0	<b>-0.009</b>	
DMC <sup>118</sup>						0	<b>-0.041</b>	
optRPA26	<b>0</b>	0.114	0.058	<b>0</b>	0.008	<b>0</b>	0.004	
	(0)	(0.106)	(0.059)					
Experiment	stable			stable		stable		

### 3.3 Surface Datasets

#### 3.3.1 Surface reactions on metals

The performance of optRPA26 was benchmarked for adsorption energies on metallic surfaces using experimental values,<sup>34,78</sup> as shown in Fig. 4. A total of 27 surface reactions were investigated on non-magnetic Cu(100), Cu(111), Ru(0001), Rh(100), Rh(111), Pd(100), Pd(111), Ir(111), and Pt(111) surfaces, as well as on the magnetic Ni(111) surface.

In Fig. 4(a), the reaction energies from ADS41 were recalculated to represent non-dissociative adsorption energies, as defined in Eq. (8). We compare the results to other density functionals as in prior sections, as well as *PBE+D3/M06*. The *PBE+D3/M06* method has been reported as one of the most accurate approaches for adsorption energy calculations, showing the lowest RMSD of 0.13 eV for the current set. The optRPA26 approach achieved a comparable accuracy with an RMSD of 0.16 eV, followed by RPA (0.25 eV). Despite substantially different computational costs, various other DFT methods showed similar accuracies with RMSDs of 0.49 eV (PBE+D3), 0.48 eV (r2SCAN+rVV10), and 0.53 eV (HSE06+D3), consistent with results from ADS41.<sup>34</sup> RPA performed significantly better than DFT methods, confirming its high accuracy for adsorption systems, as previously reported,<sup>96,120</sup> and further supported here using a larger dataset. Despite the good performance of RPA for adsorption energies, the prior benchmarking study of ethane dehydrogenation on Pt(111) showed that RPA was not superior in predicting macroscopic observables through microkinetic modeling, compared to other DFT functionals.<sup>113</sup> The reduced accuracy of these macroscopic observables is likely related to the lower accuracy of RPA for molecular energies and, in part, to the neglect of the volume dependence of molecular energies (Fig. S14).

In Fig. 4(b), the same adsorption energy results are reported using dissociative surface reaction energies, as defined in Eq. (9). The results did not change significantly, and post-DFT methods showed RMSDs of 0.13 eV (*PBE+D3/M06*), 0.13 eV (optRPA26), and 0.19 eV (RPA), while standard DFT methods exhibited RMSDs of 0.44 eV (PBE+D3), 0.46 eV

(r2SCAN+rVV10), and 0.54 eV (HSE06+D3). PBE+D3 and RPA values differed the most ( $\sim 0.05$  eV) between the two adsorption energy definitions, reflecting their large errors in molecular atomization energies, revealing a significant conflation of gas-phase and adsorbed-state errors in adsorption energies.

To deconvolute these contributions, the least-squares adsorption energies (Eq. (10)) are shown in Fig. 4(c). These adsorption energies avoid any explicit gas-phase reference by determining elemental chemical potentials by minimizing the squared magnitude of the relative reaction energies ( $E_{\text{slab+ads}} - E_{\text{slab}}$ ) in the dataset. The resulting elemental potentials will implicitly depend on the compositions of all adsorbed species, but does not rely on any computed gas-phase energies and is thus purely a dependent on the surface-adsorbate interactions.<sup>102</sup> The least-squares adsorption energies minimize bias, giving a zero mean signed error (MSD), whereas in the former two definitions, DFT methods give MSDs that are similar in magnitude to the MAD values (Fig. S16), indicating systematic error in the surface-adsorbate interactions or gas-phase energies. The strong overbinding trend is reduced when excluding the dispersion correction, leading to lower RMSDs for all DFT functionals (Fig. S16). The least-squares approach yields RMSDs of 0.12 eV (*PBE+D3/M06*), 0.11 eV (optRPA26), and 0.17 eV (RPA), with corresponding DFT errors of 0.18 eV (PBE+D3), 0.17 eV (r2SCAN+rVV10), and 0.28 eV (HSE06). The result is different if the least-squares approach is used to correct gas-phase energies only, in which case the gas-phase least-squares RMSDs are always lower than the RMSDs for adsorption energies, indicating that slab-adsorbate errors dominate for all methods (Table S3). Excluding the dispersion correction for DFT functionals leads to very similar RMSDs, confirming that the least-square approach reduces the systematic bias (Table S3). Interestingly, HSE06+D3 is consistently outperformed by other DFT methods across the different referencing schemes, likely due to issues of hybrid functionals in treating metallic systems.<sup>121,122</sup> The strong performance of *PBE+D3/M06* and optRPA26 across all referencing schemes reflects their low gas-phase errors, and suggests that methods which maximize error cancellation between gas-phase and

adsorbed species are promising for reducing adsorption energy errors.<sup>123,124</sup> However, for calculations that intrinsically involve both gas-phase and surface-mediated interactions, such as transition states of dissociative adsorption, methods like optRPA26 or *PBE+D3/M06* with inherently high gas-phase accuracy will be required.

We note a substantial difference in the adsorption energies of O and CH between our PBE+D3 values and the PBE+D3 values from Ref. 40. The energy offsets for O adsorption were consistent at 0.27–0.29 eV, with the values from Ref. 40 indicating stronger adsorption, which coincides with half of the O<sub>2</sub> energy difference between the doublet and triplet states (0.33 eV). When converting adsorption energies from Ref. 40 to the second definition, the PBE+D3 values for O adsorptions in Ref. 40 also show a similar energy shift relative to the PBE values in ADS41<sup>34</sup> (beyond D3 effects) and to the PBE+D3 values for O/Pt(111) from the literature.<sup>125,126</sup> A similar discrepancy was found for CH adsorption, with a larger energy difference of 0.59 eV. It is possible that these exaggerated adsorption energies may have propagated into the *PBE+D3/M06* values, and using the corrected energies could increase the error in the adsorption energy of the method by ∼0.3 eV for these adsorbates. However, these issues should not affect the least-squares results in Fig. 4c, where the effects of gas-phase reference states have been removed. The similar RMSDs for E<sub>ads,LS</sub> values at PBE+D3 level support this statement, with the values being 0.135 eV (Ref. 40) and 0.132 eV (our calculations). We also note a structural aspect of CH<sub>3</sub>I adsorption on Pt(111). In previous benchmarking studies of adsorption on metal surfaces,<sup>33,34,40,78</sup> CH<sub>3</sub>I was modeled as adsorbing perpendicular to Pt(111). However, experimental studies have shown that CH<sub>3</sub>I adsorbs in a tilted configuration.<sup>127–129</sup> Our DFT calculations using the tilted geometry predict that this configuration adsorbs more strongly by 0.35 eV at PBE+D3 level, compared to the perpendicular configuration. The tilted geometry is more stable with all functionals, including optRPA26, but this stronger adsorption increases error compared to experiment for functionals that already overbind CH<sub>3</sub>I, while it reduces the error for optRPA26.

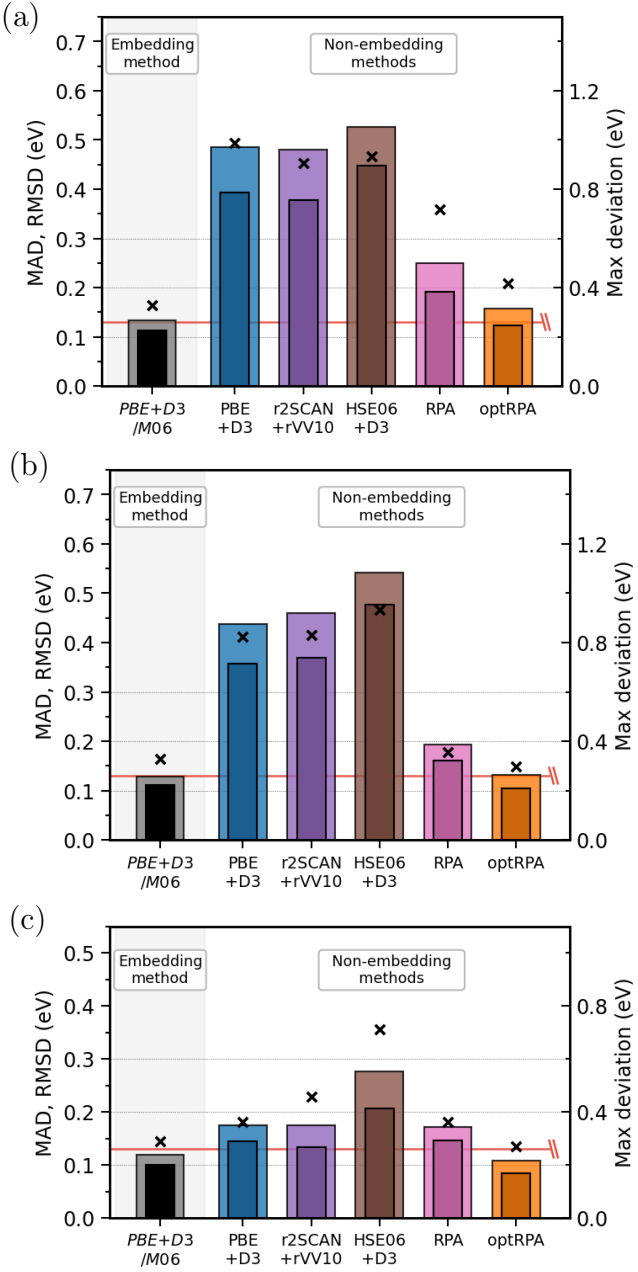


Figure 4: Absolute deviations from ZPE-corrected experimental adsorption energies<sup>40</sup> on metals (Cu, Ru, Rh, Pd, Ir, Pt, and Ni) (n=27).  $PBE+D3/M06$ <sup>40</sup> refers to a hybrid scheme that combines cluster (M06 level) and periodic model (PBE+D3 level). (a) Non-dissociative adsorption energies referenced to gas-phase adsorbates (e.g., O) as in Ref. 40. (b) Adsorption energies referenced to gas-phase molecules (e.g.,  $O_2$ ) as in ADS41.<sup>34</sup> (c) Non-dissociative adsorption energies obtained by referencing  $E(\text{slab+adsorbate}) - E(\text{slab})$  to least-squares elemental chemical potentials, compared against experimental values adjusted by the formation energies of adsorbates. The adsorption energy values are defined on a per-adsorbate basis; for example, for O adsorption, the adsorption energy is  $\Delta E$  in (a, c) or  $\Delta E/2$  in (b). Bars represent MAD (dark color) and RMSD (light color), and  $\times$  symbols indicate maximum deviations. Red horizontal lines denotes the transition metal chemical accuracy of 3 kcal/mol.

Finally, there is a well-known tradeoff between the accuracy of surface energies and adsorption energies for TM surfaces treated with standard density functionals, and RPA methods are known to perform well on both quantities.<sup>54,130</sup> To evaluate whether optRPA26 is able to simultaneously capture surface and adsorption energies, we evaluated the surface energies of four TM (Cu, Rh, Pd, and Pt) surfaces with the (111) facet and plotted them against the CO adsorption energy (used in Fig. 4a-b), as shown in Fig. 5. The post-DFT methods generally showed good agreement with experimental values of both surface and adsorption energies of CO, and optRPA26 achieved an accuracy on surface energies comparable to or better than other post-DFT methods.

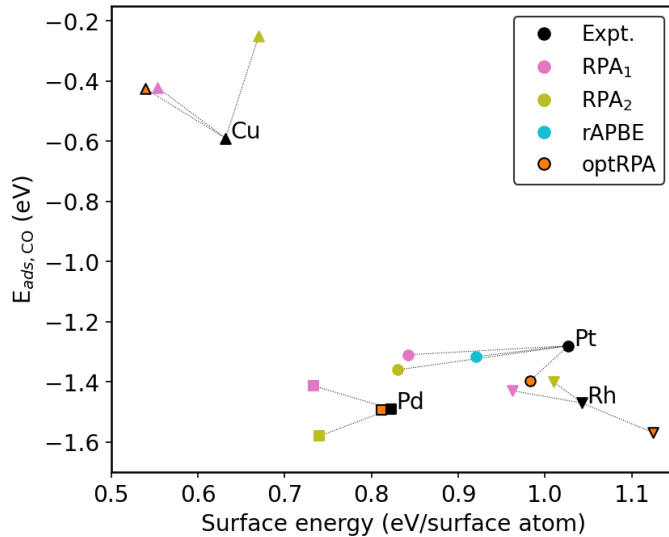


Figure 5: Surface energies and CO adsorption energies on four TM surfaces. The optRPA26 values for  $E_{ads}$  correspond to those in Fig. 4. The values of RPA<sub>1</sub>,<sup>130</sup> RPA<sub>2</sub>,<sup>96</sup> rAPBE,<sup>53</sup> and experiments<sup>79</sup> are taken from the literature.

### 3.3.2 Surface reactions on oxide

We evaluated the performance of optRPA26 for surface reactions on oxide surfaces using reference values from local CCSD(T)<sup>8,20</sup> or experiments when available (for non-dissociative H<sub>2</sub>O adsorption on MgO and TiO<sub>2</sub>),<sup>21</sup> as presented in Fig. 6. The dataset includes CO adsorption energy on MgO, and H<sub>2</sub>O adsorption and dissociation energies and barrier heights

on  $\text{Al}_2\text{O}_3$  and  $\text{TiO}_2$  surfaces. The systems were selected because both high-level energies and corresponding structures are available. A recent study of the autoSKZCAM framework<sup>21</sup> (an embedding method combining local CCSD(T)) provides high-quality structures and energies, that could serve as a basis for further benchmarking of optRPA26 in future work.

Within the set of DFT methods examined, PBE+D3 showed the lowest RMSD (0.13 eV), followed by HSE06+D3 (0.15 eV) and r2SCAN+rVV10 (0.20 eV). DFT methods significantly underestimated barrier heights for  $\text{H}_2\text{O}$  dissociation on both the  $\text{Al}_2\text{O}_3$  surface ( $E_a^{\text{CCSD(T)}}=0.38$  eV), with DFT values of 0.13 eV (PBE+D3), 0.07 eV (r2SCAN+rVV10), and 0.19 eV (HSE06+D3), and the  $\text{TiO}_2$  surface ( $E_a^{\text{CCSD(T)}}=0.32$  eV) with DFT values of 0.26 eV, 0.13 eV, and 0.17 eV, respectively. The optRPA26 method showed the lowest error metrics (MAD of 0.06 eV and RMSD of 0.08 eV), but RPA performed comparably (0.08 and 0.09 eV). These RPA-based methods yield barrier heights closer to the CCSD(T) values, namely 0.34 eV (RPA) and 0.32 eV (optRPA26) on the  $\text{Al}_2\text{O}_3$  surface, and 0.46 eV (RPA) and 0.37 eV (optRPA26) on the  $\text{TiO}_2$  surface.

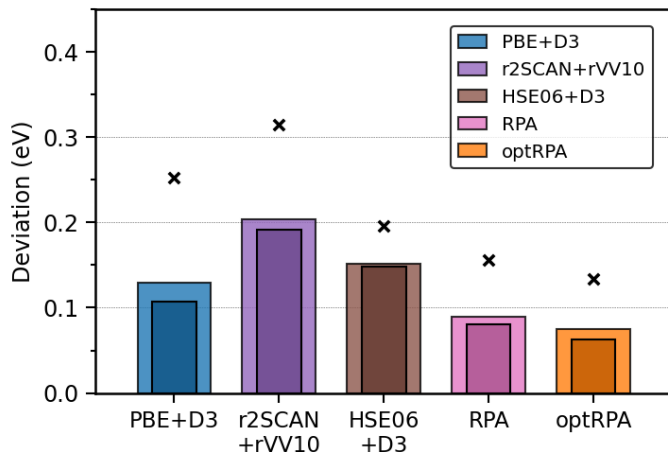


Figure 6: Absolute deviations from CCSD(T) values ( $n=5$ )<sup>8,20</sup> or ZPE-corrected experimental values ( $n=2$ ) (for  $\text{H}_2\text{O}$  adsorption on  $\text{MgO}$  and  $\text{TiO}_2$ )<sup>21</sup> for surface reaction energies on oxides ( $\text{MgO}$ ,  $\text{Al}_2\text{O}_3$ , and  $\text{TiO}_2$ ) ( $n=7$ ). Bars represent MAD (dark color) and RMSD (light color), and  $x$  symbols indicate maximum deviations.

## 4 Discussion

### 4.1 Optimization of DFT orbitals

In our previous study,<sup>57</sup> we introduced an optimized RPA method (optRPA24), which used PBEx50 (a global PBE hybrid with 50% exact exchange), to calculate DFT orbitals. Although this approach worked well for gas-phase atomization and reaction energies and for non-oxide bulk properties, further testing revealed a formation energy error exceeding 0.5 eV for the TM oxide RuO<sub>2</sub> (despite an RMSD of around 0.1 eV for formation energies of non-TM oxides). Moreover, the convergence of the PBEx50 wavefunctions was slow with respect to k-points for the adsorption energies in metals, creating a significant practical barrier to the large-scale application of optRPA24. The convergence issue is likely related to multiple local minima observed in EXX calculations of metal surfaces,<sup>24,131</sup> even with tight energy convergence thresholds ( $10^{-8}$  eV). In addition, the Coulomb singularity<sup>132</sup> worsens the energy convergence of calculations involving EXX on metals. Although singularity correction schemes have been successfully applied to approximate the  $\mathbf{G}=0$  contribution in DFT hybrid calculations,<sup>121,122</sup> RPA is far more sensitive to changes in wavefunctions, making convergence particularly challenging. Finally, we found that incorporation of EXX led to quantitative and qualitative failures in the magnetic moments of magnetic metals. For example, PBE gives a magnetic moment of 2.12  $\mu_{\text{B}}$  for bulk Fe, which is close to the experimental value of 2.13  $\mu_{\text{B}}$ ,<sup>77</sup> while hybrid functionals such as PBE0 and HSE06 predict  $\sim$ 2.8  $\mu_{\text{B}}$ , consistent with previous reports,<sup>133–135</sup> and PBEx50 predicts the same value. Also, similar to other hybrid functionals, PBEx50 incorrectly predicts the ground-state crystal structure of Co to be BCC instead of HCP, raising further questions about its suitability for treating the electronic structure of metallic systems.

Using a lower EXX fraction can alleviate some of these issues, but does not fully resolve them. Instead, we explored a long-range corrected hybrid scheme (LC) with 25% EXX to generate orbitals for RPA evaluation. Applying 25% long-range EXX did not exaggerate the

spin magnetic moment of Fe, unlike PBE0 and HSE06, which use the same EXX fraction. This behavior is consistent with the results of RSHXLDA (a long-range corrected hybrid functional with 100% EXX), where the magnetic moments of magnetic oxides were lower than PBE0 values.<sup>136</sup> In addition, using long-range EXX can destroy the Fermi surface and make a metallic system non-metallic, as observed in RSHXLDA, generating a vanishing density of states at the Fermi level in bulk Na.<sup>136</sup> This behavior can be moderated by applying a smaller fraction of EXX. For example, RSHXLDA with 25% EXX retains states at the Fermi level in bulk Na, similar to LC-srPBEx25 (Fig. S4). Nevertheless, the LC-hybrid based on the standard PBE functional required a very small range separation parameter for EXX ( $\mu < 0.5 \text{ \AA}^{-1}$ ) to reproduce the correct Fe magnetic moment. A low  $\mu$  limits the EXX contribution to only the very long-range region, substantially degrading the accuracy of RPA compared to non-LC approaches. The need for a low  $\mu$  to reproduce the correct Fe magnetic moment may stem from the incompatibility between EXX and PBE correlation.<sup>137</sup> To avoid relying on such a small  $\mu$  value, we replaced PBE with the srPBE functional,<sup>92–94</sup> specifically designed to handle short-range exchange and correlation contributions. This replacement enabled the reproduction of the correct Fe magnetic moment at a larger  $\mu$  value of  $3.0 \text{ \AA}^{-1}$ , while largely preserving the RPA accuracy. However, the use of srPBE led to incorrect orbital orderings in halogen anions, most notably in F anion, where the degeneracy of the outermost  $p$  orbitals was broken. We attribute this qualitatively incorrect orbital description to two factors. The first is insufficient exchange contribution, as only 25% EXX (only in mid- to long range) is included to prevent energy convergence failure in metallic slabs. Second, range separation is handled improperly in VASP version 6.3.2 when using Libxc functionals. In a correct scheme, the sum of GGA exchange and EXX contributions should be 100%. However, in LC-srPBEx25, GGA exchange contributes only 75% at short range ( $\mu = 0 \text{ \AA}^{-1}$ ) (instead of the expected 100%), where EXX is absent (Fig. S1(a)). We note that this issue has been partially resolved in newer versions of VASP, where an arbitrary fraction of GGA exchange can be applied, but without proper range separation for Libxc

functionals (i.e. 100% GGA exchange at  $\mu=0\text{\AA}^{-1}$ , but GGA exchange and EXX do not sum to 100% at  $\mu\neq0\text{\AA}^{-1}$ ).

We addressed this issue by increasing the srPBE correlation contribution to 500% (Fig. S1(b)), which largely compensates for the underestimation of srPBE exchange (Fig. S2). Moreover, this increase in correlation energy improved both the orbital ordering and Fe magnetic moment. The xc energy and the expectation value of xc potential of LC-srPBEx25 (75% x and 500% c) are much larger in magnitude than those of srPBE (100% x and 100% c) or a modified version of LC-srPBEx25 with 100% srPBE correlation, and are instead closer to PBE and HSE06 values (Fig. S2(a)). Although this approach of exaggerating the correlation is highly empirical and not physically justified, it fully leverages the existing implementation in VASP, one of the most widely used DFT codes, without requiring any modifications to its source code, ensuring that optRPA26 is practically accessible to any practitioner with access to VASP version 6.3.2 or greater. Despite these seemingly large modifications, the resulting charge densities from LC-srPBEx25 remained largely consistent with those obtained from other functionals (Table S1). In addition,  $\text{H}_2\text{O}$  formation energies evaluated non-self-consistently with different functionals on LC-srPBEx25 densities and orbitals were very similar to those obtained using their own self-consistent densities and orbitals (Table S2). The total energies showed similarly small differences, suggesting that the functional is physically reasonable. Although LC-srPBEx25 is highly empirical and largely ad hoc, it may help guide the development of more rigorous xc functionals with sophisticated range-separation strategies for generating RPA wavefunctions. We also re-emphasize that only the wavefunctions from the LC-srPBEx25 functional are used in optRPA26, and all energies reported ultimately use a combination of standard exact exchange energy, RPA correlation, and short-range PBE correlation as described in the Methods section.

## 4.2 Optimization of exchange and correlation parts of optRPA26

The scaling constant for the RPA correlation in optRPA26 was optimized by fitting to W4-11.<sup>61</sup> For this procedure, we used the W4-11 values provided in GMTKN55,<sup>138</sup> which are zero-point exclusive, clamped-nuclei, non-relativistic (i.e., no corrections for scalar relativistic and spin-orbit coupling effects), core-valence-corrected, designed for benchmarking of DFT functionals. However, PAW pseudopotentials in VASP are scalar relativistic and use the frozen-core approximation.<sup>80</sup> To make our results consistent with the reference values, we subtracted the scalar relativistic correction and added core-valence correction to our calculated values, leaving the original reference values unchanged. The same procedure was applied to W4-11-RE.<sup>64</sup> To improve numerical stability and magnetic properties in metallic surfaces, the non-RPA correlation part of the total energy is defined using optHXX, which combines 100% EXX and 20% srPBE correlation (with  $\mu_c=1.89 \text{ \AA}^{-1}=1.0 \text{ Bohr}^{-1}$ ). This construction is motivated by the observation that energy convergence with respect to k-points is more easily achieved when evaluating the total energy directly, rather than treating the non-RPA correlation term and RPA correlation term separately. In metallic slabs, the non-RPA correlation and RPA correlation energies tend to be highly correlated. As a result, scaling the RPA correlation energy alone—especially with large  $r_c$ —worsens the energy convergence (Fig. S8). Moreover, using a large  $r_c$  can result in physically unreasonable behavior in magnetic systems, where the spin-polarized state has a higher total energy (i.e., is more unstable) than the spin-paired state. The range separation parameter  $\mu_c$  and srPBE correlation fraction were tuned to minimize  $r_c$  while preserving most of the accuracy on the W4-11 and W4-11-RE datasets. Different choices of these two parameters did not lead to a significant change in accuracy as long as a similar  $r_c$  was obtained. Defining the non-RPA correlation part through optHXX (obtained by applying 20% srPBE correlation with  $\mu_c=1.0 \text{ Bohr}$  in the HXX calculation) reduces the optimized scaling constant from 1.114 to 1.02, indicating that the underestimation of  $E_{c,RPA}$  can be largely compensated by incorporating a fraction of GGA correlation. Alternatively, adding a fraction of srPBE or PBE correlation energy

$(E_{c,(sr)\text{PBE}})$  (or subtracting  $-V_{c,(sr)\text{PBE}} + E_{c,(sr)\text{PBE}}$ , which is printed in the VASP output) to HXX yields similar results. We note that inclusion of short-range PBE correlation is conceptually similar to the RPA+ approach,<sup>47,48</sup> although our results were similar even if full range PBE correlation is used.

### 4.3 Numerical convergence, physical accuracy, and computational cost

In standard DFT approaches it is straightforward to perform convergence testing to control numerical error associated with k-point sampling and planewave cutoff. However, these issues demand more attention when using RPA-based approaches. Despite the significantly improved k-point convergence of adsorption energies on metals with optRPA26, residual RMSDs (relative to k60 values) of less than 0.1 eV were still observed for k35–k55 meshes (Fig. S7). The total energy convergence is similar to or slightly worse than that of the adsorption energies (Fig. S8), and bulk systems tend to be more stable (Fig. S9). Magnetic slabs and 3×3 slabs exhibit poorer total energy convergence behavior, but the adsorption energy starts to converge around k40–k45. As noted earlier, this likely originates from difficulties in k-point sampling for EXX calculations involving metals with highly non-analytic Brillouin-zone integrals, where a more accurate description requires statistical sampling of k-points, for example, through twist averaging,<sup>131,139</sup> which is computationally much more demanding. A more approximate k-point sampling (i.e., averaging adsorption energies over three consecutive k-mesh scales) also helps achieve energy convergence using only coarse k-point grids (Fig. S10). When computing RPA-based adsorption energies on metals it is critical to carefully check k-point convergence and increase k-point density beyond what is typically needed for semi-local calculations; all results in the main text use a k50 mesh, which is much higher than the k20–k30 meshes typical with semi-local functionals. Conversely, oxide surfaces show significantly faster energy convergence, making it straightforward to include additional system-size correction terms, such as surface thickness and supercell size.

We also note that, when comparing to experimental values, there are other sources of uncertainty beyond the electronic structure. Uncertainty in experimental measurements for adsorption energies is typically on the order of 0.05 eV, with an average reported uncertainty of 0.07 eV.<sup>40</sup> Furthermore, physical approximations such as the precise atomic geometry of the active site and adsorbate, the number of layers in the slab, the size of the supercell and vacuum spacing, and the slab approximation itself can introduce errors that are likely also on the order of 0.05 – 0.1 eV. Finally, numerical approximations such as the pseudopotentials used<sup>140,141</sup> and the residual errors from k-point sampling, plane wave cutoff, smearing width, and FFT grid can also introduce errors of 0.01 – 0.05 eV, or higher. Taken together, it becomes difficult to differentiate signal from noise when evaluating the slow convergence with respect to k-points, and it is likely unreasonable to expect errors below  $\sim$ 0.05 – 0.1 eV when comparing to experimental adsorption energies on metals. The case of oxide surface reaction energies is more straightforward, since comparisons to other computational results eliminate the uncertainty around the structural model used, and the insulating nature of oxides makes k-point convergence much faster. Indeed, the errors of optRPA26 for oxide surface reaction energies are somewhat lower ( $\sim$ 0.08 eV), which supports that at least some of the errors in metallic adsorption energies may arise from these relatively small but uncontrolled sources of uncertainty.

It is also worth considering the computational cost of optRPA26 as compared to other commonly used methods. In general, optRPA26 calculations consist of three parts: (1) optimization of occupied bands in LC-srPBEx25 wavefunctions (via a self-consistent field (SCF) cycle), (2) one-step determination of the unoccupied bands by exact diagonalization of the KS Hamiltonian using the previous wavefunction, and (3) evaluation of the ACFDT-RPA correlation energy. The computational cost of optRPA26 is highest for metal adsorption systems. For LC-srPBEx25 calculations of a typical metal slab, one SCF iteration within an SCF cycle takes 20–100 cpu hours at k50 mesh with  $E_{\text{cutoff}}=300$  eV, whereas the cost is negligible for PBE calculations (0.1–0.2 cpu hours). The high cost of LC-srPBEx25 is

driven by the exact exchange calculation. HSE06 has an even higher computational cost of 50–300 cpu hours per SCF iteration because a larger  $E_{\text{cutoff}}$  of 600 eV was used, compared to 300 eV for LC-srPBEx25. Naturally, exact timings and performance will vary depending on computing resources, but in general the step that requires the most cpu time in optRPA26 is the SCF cycle to obtain the LC-srPBEx25 wavefunctions, while the step that requires the most memory is evaluating the RPA correlation energy.

## 5 Conclusion

We have improved the previously reported optRPA24 method to make it applicable to general systems, including magnetic metal surfaces. This improvement was achieved by fine-tuning the underlying xc functional to produce orbitals with correct non-energy properties, such as magnetic moments and orbital orderings, while also ensuring energy convergence in metallic systems. In benchmarking across diverse systems, optRPA26 showed high and well-balanced accuracy, with RMSDs of 0.06–0.16 eV. The accuracy for chemisorption at metal surfaces is particularly noteworthy, since the approach is competitive with the most accurate PBE+D3/M06 embedding method reported. This high accuracy and broad applicability for chemisorption on metals and other divers properties demonstrates the capability of optRPA24 to be used as a reference method, especially when accurate experimental data is not available and CCSD(T)-level calculations are not feasible. This study also highlights the potential of optimized RPA and related double-hybrid approaches for achieving higher accuracy than standard RPA, and suggests that further work in the development of specialized functionals for creating wavefunctions for RPA correlation calculations could enable methods that are more accurate and robust.

## Acknowledgement

A.J.M. and N.-K.Y. acknowledge funding from the U.S. Department of Energy, Office of Science, Office of Basic Energy Sciences, Chemical Sciences, Geosciences, and Biosciences Division under Award Number DE-SC0016486 and A.J.M. acknowledges further support under Grant No. DE-SC0023445. J.V. acknowledges support by the U.S. Department of Energy, Office of Science, Office of Basic Energy Sciences, Chemical Sciences, Geosciences, and Biosciences Division, Catalysis Science Program to the SUNCAT Center for Interface Science and Catalysis.

## References

- (1) Dumaz, M.; Boucher, R.; Marques, M. A.; Romero, A. H. Authorship and citation cultural nature in Density Functional Theory from solid state computational packages. *Scientometrics* **2021**, *126*, 6681–6695.
- (2) Medvedev, M. G.; Bushmarinov, I. S.; Sun, J.; Perdew, J. P.; Lyssenko, K. A. Density functional theory is straying from the path toward the exact functional. *Science* **2017**, *355*, 49–52.
- (3) DeYonker, N. J.; Peterson, K. A.; Steyl, G.; Wilson, A. K.; Cundari, T. R. Quantitative computational thermochemistry of transition metal species. *Journal of Physical Chemistry A* **2007**, *111*, 11269–11277.
- (4) Jiang, W.; Deyonker, N. J.; Determan, J. J.; Wilson, A. K. Toward accurate theoretical thermochemistry of first row transition metal complexes. *Journal of Physical Chemistry A* **2012**, *116*, 870–885.
- (5) Shee, J.; Rudshteyn, B.; Arthur, E. J.; Zhang, S.; Reichman, D. R.; Friesner, R. A. On Achieving High Accuracy in Quantum Chemical Calculations of 3 d Transition Metal-Containing Systems: A Comparison of Auxiliary-Field Quantum Monte Carlo with

Coupled Cluster, Density Functional Theory, and Experiment for Diatomic Molecules.

*Journal of Chemical Theory and Computation* **2019**, *15*, 2346–2358.

- (6) Cohen, A. J.; Mori-Sánchez, P.; Yang, W. Challenges for Density Functional Theory. *Chemical Reviews* **2012**, *112*, 289–320.
- (7) Peverati, R.; Truhlar, D. G. Quest for a universal density functional: the accuracy of density functionals across a broad spectrum of databases in chemistry and physics. *Philosophical Transactions of the Royal Society A: Mathematical, Physical and Engineering Sciences* **2014**, *372*, 20120476.
- (8) Ye, H. Z.; Berkelbach, T. C. Adsorption and vibrational spectroscopy of CO on the surface of MgO from periodic local coupled-cluster theory. *Faraday Discussions* **2024**,
- (9) Feller, D.; Peterson, K. A. Probing the limits of accuracy in electronic structure calculations: Is theory capable of results uniformly better than "chemical accuracy"? *Journal of Chemical Physics* **2007**, *126*.
- (10) Peterson, K. A.; Feller, D.; Dixon, D. A. Chemical accuracy in ab initio thermochemistry and spectroscopy: Current strategies and future challenges. *Theoretical Chemistry Accounts* **2012**, *131*.
- (11) Ripplinger, C.; Pinski, P.; Becker, U.; Valeev, E. F.; Neese, F. Sparse maps - A systematic infrastructure for reduced-scaling electronic structure methods. II. Linear scaling domain based pair natural orbital coupled cluster theory. *Journal of Chemical Physics* **2016**, *144*.
- (12) Neese, F.; Hansen, A.; Liakos, D. G. Efficient and accurate approximations to the local coupled cluster singles doubles method using a truncated pair natural orbital basis. *Journal of Chemical Physics* **2009**, *131*.

(13) Ripplinger, C.; Neese, F. An efficient and near linear scaling pair natural orbital based local coupled cluster method. *Journal of Chemical Physics* **2013**, *138*.

(14) Rolik, Z.; Szegedy, L.; Ladjánszki, I.; Ladóczki, B.; Kállay, M. An efficient linear-scaling CCSD(T) method based on local natural orbitals. *Journal of Chemical Physics* **2013**, *139*.

(15) Nagy, P. R.; Kállay, M. Optimization of the linear-scaling local natural orbital CCSD(T) method: Redundancy-free triples correction using Laplace transform. *Journal of Chemical Physics* **2017**, *146*.

(16) Nagy, P. R.; Kállay, M. Approaching the Basis Set Limit of CCSD(T) Energies for Large Molecules with Local Natural Orbital Coupled-Cluster Methods. *Journal of Chemical Theory and Computation* **2019**, *15*, 5275–5298.

(17) Ye, H. Z.; Berkelbach, T. C. Periodic Local Coupled-Cluster Theory for Insulators and Metals. *Journal of Chemical Theory and Computation* **2024**,

(18) Kubas, A.; Berger, D.; Oberhofer, H.; Maganas, D.; Reuter, K.; Neese, F. Surface Adsorption Energetics Studied with "gold Standard" Wave-Function-Based Ab Initio Methods: Small-Molecule Binding to TiO<sub>2</sub>(110). *Journal of Physical Chemistry Letters* **2016**, *7*, 4207–4212.

(19) Shi, B. X.; Zen, A.; Kapil, V.; Nagy, P. R.; Grüneis, A.; Michaelides, A. Many-Body Methods for Surface Chemistry Come of Age: Achieving Consensus with Experiments. *Journal of the American Chemical Society* **2023**, *145*, 25372–25381.

(20) Ye, H.-Z.; Berkelbach, T. C. Ab initio surface chemistry with chemical accuracy. **2024**, arXiv:2309.14640.

(21) Shi, B. X.; Rosen, A. S.; Schäfer, T.; Grüneis, A.; Kapil, V.; Zen, A.; Michaelides, A.

An accurate and efficient framework for modelling the surface chemistry of ionic materials. *Nature Chemistry* **2025**,

(22) Alavi, A.; Atalar, K.; Berkelbach, T. C.; Booth, G. H.; Chan, G. K.-L.; Evangelista, F. A.; Goldzak, T.; Grüneis, A.; Harsha, G.; Kapil, V. et al. Correlation in extended systems: general discussion. *Faraday Discussions* **2024**, *254*, 682–707.

(23) Masiros, N.; Irmler, A.; Schäfer, T.; Grüneis, A. Averting the Infrared Catastrophe in the Gold Standard of Quantum Chemistry. *Physical Review Letters* **2023**, *131*.

(24) Carbone, J. P.; Irmler, A.; Gallo, A.; Schäfer, T.; Benschoten, W. Z. V.; Shepherd, J. J.; Grüneis, A. CO adsorption on Pt(111) studied by periodic coupled cluster theory. *Faraday Discussions* **2024**, *254*, 586–597.

(25) Schäfer, T. Ground States for Metals from Converged Coupled Cluster Calculations. *The Journal of Physical Chemistry Letters* **2025**, *16*, 17–23.

(26) Needs, R. J.; Towler, M. D.; Drummond, N. D.; Ríos, P. L. Continuum variational and diffusion quantum Monte Carlo calculations. *Journal of Physics Condensed Matter* **2010**, *22*.

(27) Kim, J.; Baczewski, A. D.; Beaudet, T. D.; Benali, A.; Bennett, M. C.; Berrill, M. A.; Blunt, N. S.; Borda, E. J. L.; Casula, M.; Ceperley, D. M. et al. QMCPACK: an open source ab initio quantum Monte Carlo package for the electronic structure of atoms, molecules and solids. *Journal of Physics: Condensed Matter* **2018**, *30*, 195901.

(28) Doblhoff-Dier, K.; Meyer, J.; Hoggan, P. E.; Kroes, G. J. Quantum Monte Carlo Calculations on a Benchmark Molecule-Metal Surface Reaction:  $\text{H}_2 + \text{Cu}(111)$ . *Journal of Chemical Theory and Computation* **2017**, *13*, 3208–3219.

(29) Kent, P. R.; Annaberdiyev, A.; Benali, A.; Bennett, M. C.; Borda, E. J. L.; Doak, P.; Hao, H.; Jordan, K. D.; Krogel, J. T.; Kylänpää, I. et al. QMCPACK: Advances in

the development, efficiency, and application of auxiliary field and real-space variational and diffusion quantum Monte Carlo. *Journal of Chemical Physics* **2020**, *152*.

- (30) Krogel, J. T.; Kent, P. R. Magnitude of pseudopotential localization errors in fixed node diffusion quantum Monte Carlo. *Journal of Chemical Physics* **2017**, *146*.
- (31) Saritas, K.; Mueller, T.; Wagner, L.; Grossman, J. C. Investigation of a Quantum Monte Carlo Protocol To Achieve High Accuracy and High-Throughput Materials Formation Energies. *Journal of Chemical Theory and Computation* **2017**, *13*, 1943–1951.
- (32) Hsing, C. R.; Chang, C. M.; Cheng, C.; Wei, C. M. Quantum Monte Carlo Studies of CO Adsorption on Transition Metal Surfaces. *Journal of Physical Chemistry C* **2019**, *123*, 15659–15664.
- (33) Wellendorff, J.; Silbaugh, T. L.; Garcia-Pintos, D.; Nørskov, J. K.; Bligaard, T.; Studt, F.; Campbell, C. T. A benchmark database for adsorption bond energies to transition metal surfaces and comparison to selected DFT functionals. *Surface Science* **2015**, *640*, 36–44.
- (34) Sharada, S. M.; Karlsson, R. K.; Maimaiti, Y.; Voss, J.; Bligaard, T. Adsorption on transition metal surfaces: Transferability and accuracy of DFT using the ADS41 dataset. *Physical Review B* **2019**, *100*.
- (35) Boese, A. D.; Sauer, J. Accurate adsorption energies of small molecules on oxide surfaces: CO-MgO(001). *Physical Chemistry Chemical Physics* **2013**, *15*, 16481–16493.
- (36) Sauer, J. Ab Initio Calculations for Molecule-Surface Interactions with Chemical Accuracy. *Accounts of Chemical Research* **2019**, *52*, 3502–3510.
- (37) Alessio, M.; Usvyat, D.; Sauer, J. Chemically Accurate Adsorption Energies: CO and

H<sub>2</sub>O on the MgO(001) Surface. *Journal of Chemical Theory and Computation* **2019**, *15*, 1329–1344.

- (38) Huang, P.; Carter, E. A. Self-consistent embedding theory for locally correlated configuration interaction wave functions in condensed matter. *Journal of Chemical Physics* **2006**, *125*.
- (39) Ren, X.; Rinke, P.; Scheffler, M. Exploring the random phase approximation: Application to CO adsorbed on Cu(111). *Physical Review B - Condensed Matter and Materials Physics* **2009**, *80*.
- (40) Araujo, R. B.; Rodrigues, G. L.; dos Santos, E. C.; Pettersson, L. G. Adsorption energies on transition metal surfaces: towards an accurate and balanced description. *Nature Communications* **2022**, *13*.
- (41) Wei, Z.; Martirez, J. M. P.; Carter, E. A. Introducing the embedded random phase approximation: H<sub>2</sub> dissociative adsorption on Cu(111) as an exemplar. *Journal of Chemical Physics* **2023**, *159*.
- (42) Sheldon, C.; Paier, J.; Usyat, D.; Sauer, J. Hybrid RPA:DFT Approach for Adsorption on Transition Metal Surfaces: Methane and Ethane on Platinum (111). *Journal of Chemical Theory and Computation* **2024**, *20*, 2219–2227.
- (43) Perdew, J. P.; Ruzsinszky, A.; Tao, J.; Staroverov, V. N.; Scuseria, G. E.; Csonka, G. I. Prescription for the design and selection of density functional approximations: More constraint satisfaction with fewer fits. *Journal of Chemical Physics* **2005**, *123*.
- (44) Harl, J.; Kresse, G. Cohesive energy curves for noble gas solids calculated by adiabatic connection fluctuation-dissipation theory. *Physical Review B - Condensed Matter and Materials Physics* **2008**, *77*.

(45) Furche, F.; Voorhis, T. V. Fluctuation-dissipation theorem density-functional theory. *Journal of Chemical Physics* **2005**, *122*.

(46) Olsen, T.; Thygesen, K. S. Random phase approximation applied to solids, molecules, and graphene-metal interfaces: From van der Waals to covalent bonding. *Physical Review B - Condensed Matter and Materials Physics* **2013**, *87*.

(47) Yan, Z.; Perdew, J. P.; Kurth, S. Density functional for short-range correlation: Accuracy of the random-phase approximation for isoelectronic energy changes. *Physical Review B* **2000**, *61*, 16430–16439.

(48) Gould, T.; Ruzsinszky, A.; Perdew, J. P. Simple self-interaction correction to random-phase-approximation-like correlation energies. *Physical Review A* **2019**, *100*.

(49) Grüneis, A.; Marsman, M.; Harl, J.; Schimka, L.; Kresse, G. Making the random phase approximation to electronic correlation accurate. *Journal of Chemical Physics* **2009**, *131*.

(50) Paier, J.; Ren, X.; Rinke, P.; Scuseria, G. E.; Grüneis, A.; Kresse, G.; Scheffler, M. Assessment of correlation energies based on the random-phase approximation. *New Journal of Physics* **2012**, *14*.

(51) Ren, X.; Rinke, P.; Scuseria, G. E.; Scheffler, M. Renormalized second-order perturbation theory for the electron correlation energy: Concept, implementation, and benchmarks. *Physical Review B - Condensed Matter and Materials Physics* **2013**, *88*.

(52) Ruzsinszky, A.; Zhang, I. Y.; Scheffler, M. Insight into organic reactions from the direct random phase approximation and its corrections. *Journal of Chemical Physics* **2015**, *143*.

(53) Olsen, T.; Thygesen, K. S. Accurate ground-state energies of solids and molecules from time-dependent density-functional theory. *Physical Review Letters* **2014**, *112*.

(54) Olsen, T.; Patrick, C. E.; Bates, J. E.; Ruzsinszky, A.; Thygesen, K. S. Beyond the RPA and GW methods with adiabatic xc-kernels for accurate ground state and quasi-particle energies. *npj Computational Materials* **2019**, *5*, 106.

(55) Ruzsinszky, A.; Perdew, J. P.; Csonka, G. I. The RPA atomization energy puzzle. *Journal of Chemical Theory and Computation* **2010**, *6*, 127–134.

(56) Furche, F.; Voorhis, T. V. Fluctuation-dissipation theorem density-functional theory. *The Journal of Chemical Physics* **2005**, *122*.

(57) Kim, H.; Yu, N.-K.; Tian, N.; Medford, A. J. Assessing Exchange-Correlation Functionals for Heterogeneous Catalysis of Nitrogen Species. *The Journal of Physical Chemistry C* **2024**, *128*, 11159–11175.

(58) Janesko, B. G.; Henderson, T. M.; Scuseria, G. E. Long-range-corrected hybrids including random phase approximation correlation. *Journal of Chemical Physics* **2009**, *130*.

(59) Irelan, R. M.; Henderson, T. M.; Scuseria, G. E. Long-range-corrected hybrids using a range-separated Perdew-Burke-Ernzerhof functional and random phase approximation correlation. *Journal of Chemical Physics* **2011**, *135*.

(60) Lehtola, S.; Steigemann, C.; Oliveira, M. J.; Marques, M. A. Recent developments in LIBXC — A comprehensive library of functionals for density functional theory. *SoftwareX* **2018**, *7*, 1–5.

(61) Karton, A.; Daon, S.; Martin, J. M. W4-11: A high-confidence benchmark dataset for computational thermochemistry derived from first-principles W4 data. *Chemical Physics Letters* **2011**, *510*, 165–178.

(62) Karton, A.; Rabinovich, E.; Martin, J. M.; Ruscic, B. W4 theory for computational

thermochemistry: In pursuit of confident sub-kJ/mol predictions. *Journal of Chemical Physics* **2006**, *125*.

(63) cis/trans-HO<sub>3</sub>, Be<sub>2</sub>, B<sub>2</sub>, C<sub>2</sub>, BN, OF, F<sub>2</sub>O, FOO, FOOF, Cl<sub>2</sub>O, ClOO, OC<sub>1</sub>O, O<sub>3</sub>, S<sub>3</sub>, and S<sub>4</sub>.

(64) Margraf, J. T.; Ranasinghe, D. S.; Bartlett, R. J. Automatic generation of reaction energy databases from highly accurate atomization energy benchmark sets. *Physical Chemistry Chemical Physics* **2017**, *19*, 9798–9805.

(65) Zhao, Y.; Lynch, B. J.; Truhlar, D. G. Multi-coefficient extrapolated density functional theory for thermochemistry and thermochemical kinetics. *Physical Chemistry Chemical Physics* **2005**, *7*, 43–52.

(66) Zhao, Y.; González-Garda, N.; Truhlar, D. G. Benchmark database of barrier heights for heavy atom transfer, nucleophilic substitution, association, and unimolecular reactions and its use to test theoretical methods. *Journal of Physical Chemistry A* **2005**, *109*, 2012–2018.

(67) Goerigk, L.; Grimme, S. A general database for main group thermochemistry, kinetics, and noncovalent interactions - Assessment of common and reparameterized (meta-)GGA density functionals. *Journal of Chemical Theory and Computation* **2010**, *6*, 107–126.

(68) Iron, M. A.; Janes, T. Evaluating Transition Metal Barrier Heights with the Latest Density Functional Theory Exchange-Correlation Functionals: The MOBH35 Benchmark Database. *Journal of Physical Chemistry A* **2019**, *123*, 3761–3781.

(69) Dohm, S.; Bursch, M.; Hansen, A.; Grimme, S. Semiautomated Transition State Localization for Organometallic Complexes with Semiempirical Quantum Chemical Methods. *Journal of Chemical Theory and Computation* **2020**, *16*, 2002–2012.

(70) Semidalas, E.; Martin, J. M. The MOBH35 Metal-Organic Barrier Heights Reconsidered: Performance of Local-Orbital Coupled Cluster Approaches in Different Static Correlation Regimes. *Journal of Chemical Theory and Computation* **2022**, *18*, 883–898.

(71) Grotjahn, R.; Kaupp, M. A Look at Real-World Transition-Metal Thermochemistry and Kinetics with Local Hybrid Functionals. *Israel Journal of Chemistry* **2023**, *63*.

(72) Řezáč, J.; Riley, K. E.; Hobza, P. S66: A well-balanced database of benchmark interaction energies relevant to biomolecular structures. *Journal of Chemical Theory and Computation* **2011**, *7*, 2427–2438.

(73) Harl, J.; Schimka, L.; Kresse, G. Assessing the quality of the random phase approximation for lattice constants and atomization energies of solids. *Physical Review B - Condensed Matter and Materials Physics* **2010**, *81*.

(74) Zhang, G. X.; Reilly, A. M.; Tkatchenko, A.; Scheffler, M. Performance of various density-functional approximations for cohesive properties of 64 bulk solids. *New Journal of Physics* **2018**, *20*.

(75) Yan, J.; Hummelshøj, J. S.; Nørskov, J. K. Formation energies of group i and II metal oxides using random phase approximation. *Physical Review B - Condensed Matter and Materials Physics* **2013**, *87*.

(76) Voss, J. Hubbard-corrected oxide formation enthalpies without adjustable parameters. *Journal of Physics Communications* **2022**, *6*, 035009.

(77) Wijn, H. In *3d, 4d and 5d Elements, Alloys and Compounds*; Wijn, H. P. J., Ed.; Springer-Verlag, 1997; Vol. 32A; p 41.

(78) Duanmu, K.; Truhlar, D. G. Validation of Density Functionals for Adsorption Energies

on Transition Metal Surfaces. *Journal of Chemical Theory and Computation* **2017**, *13*, 835–842.

(79) Vitos, L.; Ruban, A.; Skriver, H.; Kollár, J. The surface energy of metals. *Surface Science* **1998**, *411*, 186–202.

(80) Kresse, G.; Hafner, J. Ab initio molecular dynamics for liquid metals. *Physical Review B* **1993**, *47*, 558–561.

(81) Kresse, G.; Furthmüller, J. Efficient iterative schemes for ab initio total-energy calculations using a plane-wave basis set. *Physical Review B* **1996**, *54*, 11169–11186.

(82) Kresse, G.; Furthmüller, J. Efficiency of ab-initio total energy calculations for metals and semiconductors using a plane-wave basis set. *Computational Materials Science* **1996**, *6*, 15–50.

(83) Kresse, G.; Joubert, D. From ultrasoft pseudopotentials to the projector augmented-wave method. *Physical Review B* **1999**, *59*, 1758–1775.

(84) Available PAW pseudopotentials in VASP. [https://www.vasp.at/wiki/index.php/Available\\_pseudopotentials](https://www.vasp.at/wiki/index.php/Available_pseudopotentials).

(85) Perdew, J. P.; Burke, K.; Ernzerhof, M. Generalized Gradient Approximation Made Simple. *Physical Review Letters* **1996**, *77*, 3865–3868.

(86) Grimme, S.; Ehrlich, S.; Goerigk, L. Effect of the damping function in dispersion corrected density functional theory. *Journal of Computational Chemistry* **2011**, *32*, 1456–1465.

(87) Sabatini, R.; Gorni, T.; Gironcoli, S. D. Nonlocal van der Waals density functional made simple and efficient. *Physical Review B - Condensed Matter and Materials Physics* **2013**, *87*.

(88) Galimberti, D. R.; Sauer, J. Chemically Accurate Vibrational Free Energies of Adsorption from Density Functional Theory Molecular Dynamics: Alkanes in Zeolites. *Journal of Chemical Theory and Computation* **2021**, *17*, 5849–5862.

(89) Ning, J.; Kothakonda, M.; Furness, J. W.; Kaplan, A. D.; Ehlert, S.; Brandenburg, J. G.; Perdew, J. P.; Sun, J. Workhorse minimally empirical dispersion-corrected density functional with tests for weakly bound systems: R2SCAN+rVV10. *Physical Review B* **2022**, *106*.

(90) Krukau, A. V.; Vydrov, O. A.; Izmaylov, A. F.; Scuseria, G. E. Influence of the exchange screening parameter on the performance of screened hybrid functionals. *Journal of Chemical Physics* **2006**, *125*.

(91) Kaltak, M.; Klimeš, J.; Kresse, G. Cubic scaling algorithm for the random phase approximation: Self-interstitials and vacancies in Si. *Physical Review B - Condensed Matter and Materials Physics* **2014**, *90*.

(92) Toulouse, J.; Colonna, F.; Savin, A. Short-range exchange and correlation energy density functionals: Beyond the local-density approximation. *Journal of Chemical Physics* **2005**, *122*.

(93) Goll, E.; Werner, H. J.; Stoll, H. A short-range gradient-corrected density functional in long-range coupled-cluster calculations for rare gas dimers. *Physical Chemistry Chemical Physics* **2005**, *7*, 3917–3923.

(94) Goll, E.; Werner, H. J.; Stoll, H.; Leininger, T.; Gori-Giorgi, P.; Savin, A. A short-range gradient-corrected spin density functional in combination with long-range coupled-cluster methods: Application to alkali-metal rare-gas dimers. *Chemical Physics* **2006**, *329*, 276–282.

(95) Jauho, T. S.; Olsen, T.; Bligaard, T.; Thygesen, K. S. Improved description of metal

oxide stability: Beyond the random phase approximation with renormalized kernels.

*Physical Review B - Condensed Matter and Materials Physics* **2015**, 92.

(96) Schmidt, P. S.; Thygesen, K. S. Benchmark Database of Transition Metal Surface and Adsorption Energies from Many-Body Perturbation Theory. *Journal of Physical Chemistry C* **2018**, 122, 4381–4390.

(97) Sheldon, C.; Paier, J.; Sauer, J. Adsorption of CH<sub>4</sub> on the Pt(111) surface: Random phase approximation compared to density functional theory. *Journal of Chemical Physics* **2021**, 155.

(98) Oudot, B.; Doblhoff-Dier, K. Reaction barriers at metal surfaces computed using the random phase approximation: Can we beat DFT in the generalized gradient approximation? *Journal of Chemical Physics* **2024**, 161.

(99) Schäfer, T.; Daelman, N.; López, N. Cerium Oxides without U: The Role of Many-Electron Correlation. *Journal of Physical Chemistry Letters* **2021**, 12, 6277–6283.

(100) Gygi, F.; Baldereschi, A. Self-consistent Hartree-Fock and screened-exchange calculations in solids: Application to silicon. *Physical Review B* **1986**, 34, 4405–4408.

(101) Massidda, S.; Posternak, M.; Baldereschi, A. Hartree-Fock LAPW approach to the electronic properties of periodic systems. *Physical Review B* **1993**, 48, 5058–5068.

(102) Kreitz, B.; Gusmão, G. S.; Nai, D.; Sahoo, S. J.; Peterson, A. A.; Bross, D. H.; Goldsmith, C. F.; Medford, A. J. Unifying thermochemistry concepts in computational heterogeneous catalysis. 2024.

(103) Ruscic, B.; Bross, D. Active Thermochemical Tables (ATcT) values based on ver. 1.220 of the Thermochemical Network.

(104) Irikura, K. K. Experimental vibrational zero-point energies: Diatomic molecules. *Journal of Physical and Chemical Reference Data* **2007**, 36, 389–397.

(105) Shin, H.; Kang, S.; Koo, J.; Lee, H.; Kim, J.; Kwon, Y. Cohesion energetics of carbon allotropes: Quantum Monte Carlo study. *Journal of Chemical Physics* **2014**, *140*.

(106) Khiri, D.; Černušák, I.; Louis, F. Theoretical Study of the Reactions of H Atoms with CH<sub>3</sub>I and CH<sub>2</sub>I<sub>2</sub>. *Journal of Physical Chemistry A* **2018**, *122*, 6546–6557.

(107) NIST Computational Chemistry Comparison and Benchmark Database, NIST Standard Reference Database Number 101 Release 22, May 2022, Editor: Russell D. Johnson III .<http://cccbdb.nist.gov/>.

(108) Karp, E. M.; Silbaugh, T. L.; Campbell, C. T. Energetics of adsorbed CH<sub>3</sub> on Pt(111) by calorimetry. *Journal of the American Chemical Society* **2013**, *135*, 5208–5211.

(109) Wolcott, C. A.; Green, I. X.; Silbaugh, T. L.; Xu, Y.; Campbell, C. T. Energetics of adsorbed CH<sub>2</sub> and CH on Pt(111) by calorimetry: The dissociative adsorption of diiodomethane. *Journal of Physical Chemistry C* **2014**, *118*, 29310–29321.

(110) Isaacs, E. B.; Shin, H.; Annaberdiyev, A.; Wolverton, C.; Mitas, L.; Benali, A.; Heinonen, O. Assessing the accuracy of compound formation energies with quantum Monte Carlo. *Physical Review B* **2022**, *105*.

(111) Neese, F. The ORCA program system. *Wiley Interdisciplinary Reviews: Computational Molecular Science* **2012**, *2*, 73–78.

(112) Weigend, F.; Ahlrichs, R. Balanced basis sets of split valence, triple zeta valence and quadruple zeta valence quality for H to Rn: Design and assessment of accuracy. *Physical Chemistry Chemical Physics* **2005**, 3297–3305.

(113) Szaro, N. A.; Bello, M.; Fricke, C. H.; Bamidele, O. H.; Heyden, A. Benchmarking the Accuracy of Density Functional Theory against the Random Phase Approximation for the Ethane Dehydrogenation Network on Pt(111). *Journal of Physical Chemistry Letters* **2023**, *14*, 10769–10778.

(114) Patrick, C. E.; Thygesen, K. S. Adiabatic-connection fluctuation-dissipation DFT for the structural properties of solids - The renormalized ALDA and electron gas kernels. *Journal of Chemical Physics* **2015**, *143*.

(115) Jang, Y. R.; Yu, B. D. Hybrid functional study of the structural and electronic properties of Co and Ni. *Journal of the Physical Society of Japan* **2012**, *81*.

(116) Labat, F.; Baranek, P.; Domain, C.; Minot, C.; Adamo, C. Density functional theory analysis of the structural and electronic properties of TiO<sub>2</sub> rutile and anatase polytypes: Performances of different exchange-correlation functionals. *Journal of Chemical Physics* **2007**, *126*.

(117) Zhang, T.; Yang, X.; Ge, Q. Surface chemistry and reactivity of  $\{\alpha\}$ -MoO<sub>3</sub> toward methane: A SCAN-functional based DFT study. *Journal of Chemical Physics* **2019**, *151*.

(118) Luo, Y.; Benali, A.; Shulenburger, L.; Krogel, J. T.; Heinonen, O.; Kent, P. R. Phase stability of TiO<sub>2</sub> polymorphs from diffusion Quantum Monte Carlo. *New Journal of Physics* **2016**, *18*.

(119) Fox, S.; Jansen, H. J. F. Total energy of trigonal and tetragonal cobalt. *Physical Review B* **1999**, *60*, 4397–4400.

(120) Sauer, J. The future of computational catalysis. *Journal of Catalysis* **2024**, *433*.

(121) Spencer, J.; Alavi, A. Efficient calculation of the exact exchange energy in periodic systems using a truncated Coulomb potential. *Physical Review B - Condensed Matter and Materials Physics* **2008**, *77*.

(122) Sundararaman, R.; Arias, T. A. Regularization of the Coulomb singularity in exact exchange by Wigner-Seitz truncated interactions: Towards chemical accuracy in non-

trivial systems. *Physical Review B - Condensed Matter and Materials Physics* **2013**, *87*.

(123) Kreitz, B.; Abeywardane, K.; Goldsmith, C. F. Linking Experimental and Ab Initio Thermochemistry of Adsorbates with a Generalized Thermochemical Hierarchy. *Journal of Chemical Theory and Computation* **2023**, *19*, 4149–4162.

(124) Porter, S. G.; Kreitz, B. Thermophysical properties of adsorbates with beyond-DFT accuracy from DFT data through error cancellation. *Faraday Discussions* **2026**,

(125) Gautier, S.; Steinmann, S. N.; Michel, C.; Fleurat-Lessard, P.; Sautet, P. Molecular adsorption at Pt(111). How accurate are DFT functionals? *Physical Chemistry Chemical Physics* **2015**, *17*, 28921–28930.

(126) Wexler, R. B.; Carter, E. A. Oxygen-Chlorine Chemisorption Scaling for Seawater Electrolysis on Transition Metals: The Role of Redox. *Advanced Theory and Simulations* **2023**, *6*.

(127) Zaera, F.; Hoffmann, H. Detection of chemisorbed methyl and methylene groups: surface chemistry of methyl iodide on platinum(111). *The Journal of Physical Chemistry* **1991**, *95*, 6297–6303.

(128) Fan, J.; Trenary, M. Symmetry and the Surface Infrared Selection Rule for the determination of the Structure of Molecules on Metal Surfaces. *Langmuir* **1994**, *10*, 3649–3657.

(129) French, C.; Harrison, I. Orientation and decomposition kinetics of methyl iodide on Pt(111). *Surface Science* **1995**, *342*, 85–100.

(130) Schimka, L.; Harl, J.; Stroppa, A.; Grüneis, A.; Marsman, M.; Mittendorfer, F.; Kresse, G. Accurate surface and adsorption energies from many-body perturbation theory. *Nature Materials* **2010**, *9*, 741–744.

(131) Mihm, T. N.; Schäfer, T.; Ramadugu, S. K.; Weiler, L.; Grüneis, A.; Shepherd, J. J. A shortcut to the thermodynamic limit for quantum many-body calculations of metals. *Nature Computational Science* **2021**, *1*, 801–808.

(132) Ashcroft, N. W.; Mermin, N. D. *Solid State Physics*; Saunders College Publishing, 1976; p 337.

(133) Tran, F.; Baudesson, G.; Carrete, J.; Madsen, G. K.; Blaha, P.; Schwarz, K.; Singh, D. J. Shortcomings of meta-GGA functionals when describing magnetism. *Physical Review B* **2020**, *102*.

(134) Jana, S.; Patra, A.; Constantin, L. A.; Samal, P. Screened range-separated hybrid by balancing the compact and slowly varying density regimes: Satisfaction of local density linear response. *Journal of Chemical Physics* **2020**, *152*.

(135) Voss, J. Machine learning for accuracy in density functional approximations. *Journal of Computational Chemistry* **2024**, *45*, 1829–1845.

(136) Gerber, I. C.; Ángyán, J. G.; Marsman, M.; Kresse, G. Range separated hybrid density functional with long-range Hartree-Fock exchange applied to solids. *Journal of Chemical Physics* **2007**, *127*.

(137) Chai, J. D.; Head-Gordon, M. Systematic optimization of long-range corrected hybrid density functionals. *Journal of Chemical Physics* **2008**, *128*.

(138) Goerigk, L.; Hansen, A.; Bauer, C.; Ehrlich, S.; Najibi, A.; Grimme, S. A look at the density functional theory zoo with the advanced GMTKN55 database for general main group thermochemistry, kinetics and noncovalent interactions. *Physical Chemistry Chemical Physics* **2017**, *19*, 32184–32215.

(139) Lin, C.; Zong, F. H.; Ceperley, D. M. Twist-averaged boundary conditions in con-

tinuum quantum Monte Carlo algorithms. *Physical Review E - Statistical Physics, Plasmas, Fluids, and Related Interdisciplinary Topics* **2001**, *64*, 12.

- (140) Lejaeghere, K.; Bihlmayer, G.; Björkman, T.; Blaha, P.; Blügel, S.; Blum, V.; Caliste, D.; Castelli, I. E.; Clark, S. J.; Corso, A. D. et al. Reproducibility in density functional theory calculations of solids. *Science* **2016**, *351*.
- (141) Borlido, P.; Doumont, J.; Tran, F.; Marques, M. A.; Botti, S. Validation of Pseudopotential Calculations for the Electronic Band Gap of Solids. *Journal of Chemical Theory and Computation* **2020**, *16*, 3620–3627.
- (142) Olsen, T.; Thygesen, K. S. Beyond the random phase approximation: Improved description of short-range correlation by a renormalized adiabatic local density approximation. *Physical Review B - Condensed Matter and Materials Physics* **2013**, *88*.
- (143) Jain, A.; Ong, S. P.; Hautier, G.; Chen, W.; Richards, W. D.; Dacek, S.; Cholia, S.; Gunter, D.; Skinner, D.; Ceder, G. et al. Commentary: The Materials Project: A materials genome approach to accelerating materials innovation. *APL Materials* **2013**, *1*.

# Supporting Information Available

## 1 Supporting Information

### 1.1 Details of Benchmark Datasets

#### 1.1.1 Molecular datasets

The datasets for molecules include subsets of W4-11 (molecular atomization energy)<sup>61</sup> and W4-11-RE (reaction energies derived from W4-11),<sup>64</sup> BH76 (barrier heights of molecular reactions),<sup>65–67</sup> BH76RC (reaction energies derived from BH76),<sup>67</sup> MOBH29 (barrier heights and reaction energies of transition metal (TM) complexes),<sup>68–71</sup> and the S19 subset of S66 (non-covalent interaction energies of molecular complexes).<sup>72</sup> W4-11, BH76, BH76RC, and S66 are subsets of the GMTKN55 benchmark database,<sup>138</sup> whose values were used as reference values in this study. Charge and multiplicity values reported in the datasets were used.

The **W4-11** dataset contains 140 atomization energies of small first- and second-row molecules and radicals.<sup>61</sup> The reference energies were calculated using highly accurate W4 theory, which includes post-CCSD(T) contributions.<sup>62</sup> Its superior accuracy, along with the fact that error cancellation is less likely in atomization energies than in reaction energies, makes it well suited for optimizing the scaling constant for RPA correlation energy. In W4-11, we only considered 124 molecules with less multireference character (TAE\_nonMR124 subset of W4-11<sup>61</sup>), which should be more relevant for catalysis. The excluded molecules include C<sub>2</sub>, FOOF, and S<sub>4</sub>, and a complete list can be found in Ref. 63. The **W4-11-RE** dataset,<sup>64</sup> derived from W4-11, contains 11,247 reaction energies. Similarly to W4-11, we selected only reactions involving molecules in TAE\_nonMR124, resulting in 8,868 reactions. The **BH76** dataset contains 76 barrier heights of hydrogen transfer, heavy atom transfer, nucleophilic substitution, unimolecular and association reactions.<sup>65–67</sup> The **BH76RC** dataset, derived from BH76, consists of 30 reaction energies.<sup>67</sup> The **MOBH29** dataset, which is a revised

version of MOBH35,<sup>68</sup> contains 29 forward and 29 backward barrier heights, as well as 29 reaction energies of organometallic TM complexes.<sup>68–71</sup> MOBH29 does not contain reactions 17–20 and 24–25 from the original dataset, and reference values were obtained from Ref. 70. The S66 dataset contains 66 interaction energies of biomolecules containing H, C, N, and O elements.<sup>72</sup> We considered the **S19** subset, introduced in this work and derived from the original S66 set,<sup>72</sup> which includes 19 interaction energies. Of these, 14 data points were selected based on the 10 worst-performing cases for each DFT functional considered in this study.

### 1.1.2 Bulk solid datasets

For bulk solids, we considered datasets containing 24 lattice constants, 24 bulk moduli, and 24 atomization energies of non-oxides,<sup>53,73,114,142</sup> as well as a dataset of 23 oxide formation energies.<sup>75,76,95</sup> For reference values of bulk moduli, zero-point energy (ZPE)-corrected values from a previous study were used.<sup>74</sup> The oxide formation dataset includes all data points from Ref. 75, except for  $\text{LiO}_2$ , whose most stable form was not available in the Materials Project,<sup>143</sup> and it includes one additional TM oxide,  $\text{MoO}_3$ .<sup>76</sup>

We also tested the magnetic moments of magnetic solids (Fe, Co, and Ni) and examined the relative stability of bulk phases of Co (hcp, fcc, and bcc phases),  $\text{MoO}_3$  ( $\alpha$  and  $\beta$  phases), and  $\text{TiO}_2$  (rutile and anatase phases), as DFT (or specific functionals) fails to predict the correct ground-state phase.<sup>115–117</sup>

### 1.1.3 Surface datasets

We considered surface reactions involving metal and oxide surfaces, as well as surface energies of selected metals. For surface reactions on metals, we used a subset of the ADS41 dataset,<sup>34</sup> which includes CE39<sup>33</sup> and contains 41 experimental adsorption energies, and selected 27 data points for evaluation.

For surface reactions on oxide surfaces, seven reactions on  $\text{MgO}$ ,  $\text{Al}_2\text{O}_3$ , and  $\text{TiO}_2$  sur-

faces were examined using CCSD(T)-level reference values<sup>8,20</sup> and two experimental values (for non-dissociative H<sub>2</sub>O adsorption on MgO and TiO<sub>2</sub>).<sup>21</sup> Here, adsorption energies were evaluated using the second definition, with the energies referenced to a gas-phase reactant (CO or H<sub>2</sub>O).

Surface energies were evaluated for four transition metal (Cu, Rh, Pd, and Pt) surfaces with (111) orientation. Data from experiment<sup>79</sup> and other RPA-based methods<sup>54,96,130</sup> were taken directly from literature sources.

## 1.2 Dataset-Specific Computational Details

### 1.2.1 Settings for molecular datasets

For the RPA calculations of molecules, a single  $\Gamma$ -point and  $E_{\text{cutoff}}$  of 600 eV were used, except for MOBH29. All DFT calculations used the same  $E_{\text{cutoff}}$  of 600 eV. Gaussian smearing was applied with a smearing width of 0.001 eV. The molecular structures from the original datasets were used. Each molecule was placed in a 10 Å cubic cell, except for MOBH29 and S66. Due to the large molecular sizes in MOBH29, the molecules were placed in a larger cubic cell (14.5 Å) and rotated to ensure that the minimum distance between any two atoms in adjacent periodic images was larger than 5.5 Å, with  $E_{\text{cutoff}}$  set to 500 eV for RPA calculations only. Similarly, for S66, a larger cubic cell (12 Å) was used to maintain a minimum inter-image atom–atom distance of 6 Å.

### 1.2.2 Settings for bulk solid datasets

Gaussian smearing was applied with a smearing width of 0.01 eV. The  $\Gamma$ -point-centered  $k$ -point grids were generated using a density-based scheme equivalent to `KSPACING` in VASP, defined as  $\max(1, \text{ceil}(2\pi \cdot |\mathbf{b}_i|/d_k))$ , where  $\mathbf{b}_i$  is the reciprocal lattice vector,  $d_k$  is the target  $k$ -point effective length scale (in Å<sup>-1</sup>), and  $\text{ceil}(x)$  returns the smallest integer greater than or equal to  $x$ . The  $k$ -point density is defined as  $1/d_k$  (in Å).

For non-oxide solids, we used  $E_{\text{cutoff}}$  of 600 eV and  $k$ -point densities of 3.2 Å for insulators and 4.5 Å for metals to calculate lattice constants, bulk moduli, and atomization energies in both DFT and RPA calculations. When evaluating  $E_{\text{optHXX}}$ , the FFT grid for the exact exchange was set to “Accurate” to ensure more reliable energy derivatives for computing the bulk modulus. The reported lattice constants and bulk moduli were obtained by fitting the Birch–Murnaghan equation of state to energies computed at seven volumes centered around the experimental values (spanning 90–110%). The atomization energies were evaluated using the structures corresponding to the fitted lattice constants.

Oxide formation energies were calculated using PBE+D3-optimized structures for all systems involved. The  $\Delta$ cutoff was applied for the calculation of oxide formation energy. The “low-k” and “high-k” in Eqs. (6–7) correspond to k-point densities of  $2.0 \text{ \AA}^{-1}$  and  $4.0 \text{ \AA}^{-1}$  for oxides, and  $3.0 \text{ \AA}^{-1}$  and  $6.0 \text{ \AA}^{-1}$  for metals, respectively. The “low-E” value corresponds to  $E_{\text{cutoff}}$  of 400 eV, and “high-E” values are 900 eV (for exchange) and 600 eV (for correlation). DFT calculations were performed using the “high-k” and “high-E” (for exchange).

### 1.2.3 Settings for surface datasets

Unlike in bulk calculations, the k-point grids here are defined using a k-mesh scale, based on real-space supercell dimensions. For example, the k-mesh scale “k35” corresponds to a k35 mesh or a  $\Gamma$ -point-centered k-point grid of  $[\text{round}(35/A), \text{round}(35/B), 1]$ , where  $A$  and  $B$  are the x and y dimensions of the supercell and round denotes rounding to the nearest integer.

For most surface reactions on metals, the calculations employed  $2 \times 2$ , four-layer slabs with a vacuum spacing of  $13.5 \text{ \AA}$ . The reactions involving O/Pt(111) and  $\text{C}_3\text{H}_8/\text{Pt}(111)$  were calculated using  $3 \times 3$  slabs. The surface structures were optimized using PBE+D3, with the two bottom layers fixed. Gaussian smearing was applied with smearing widths of 0.1 eV (for DFT) and 0.01 eV (for RPA). The  $\Delta$ cutoff was applied for RPA calculations. The “low-k” and “high-k” correspond to k35 (or k25 for  $3 \times 3$  slabs) and k50 meshes. The k50 mesh corresponds to k-point densities of 6–7.5  $\text{ \AA}^{-1}$ . The “low-E” and “high-E” correspond to  $E_{\text{cutoff}}$  values of 300 eV and 500 eV. Results of the convergence tests can be found in Fig. S5 ( $E_{\text{cutoff}}$ ), Fig. S6 (smearing width), and Fig. S7 (k-point). DFT calculations were conducted using k50 mesh and  $E_{\text{cutoff}}$  of 600 eV.

For oxide surfaces, we used structures from the literature from which the CCSD(T) reference values were obtained<sup>8,20</sup> and applied a vacuum spacing of 13  $\text{ \AA}$ . The  $\Delta$ cutoff was applied for RPA calculations. The “low-k” corresponds to k1 mesh, while “high-k” corresponds to k20 (for  $\text{TiO}_2$ ) and k25 meshes (for  $\text{MgO}$  and  $\text{Al}_2\text{O}_3$ ). The “low-E” is 400 eV, and “high-E” values

are 900 eV (for exchange) and 600 eV (for correlation). DFT calculations were performed using the “high-k” and “high-E” (for exchange). More details about the structures, as well as an additional correction term for slab thickness ( $\Delta_{layer} < 0.05$  eV) (applied to MgO and  $\text{TiO}_2$ ) and for supercell size ( $\Delta_{supercell} \sim 0.01$  eV) (applied to MgO) are provided in the Oxide surface section of the SI. The results of energy convergence can be found in Fig. S11 and S12.

For metal surface energies, PBE+D3-optimized bulk and surface structures were used. The surface models consisted of  $1 \times 1$  six-layer slabs, with the two middle layers fixed during structural relaxation. The  $\Delta_{cutoff}$  was applied for both bulk and surface systems. For bulk calculations, the “low-k” and “high-k” correspond to k-point densities of 3.0 Å and 7.0 Å. For surface, “low-k” and “high-k” are k35 and k80 meshes. For both systems, “low-E” and “high-E” correspond to  $E_{cutoff}$  values of 300 eV and 500 eV. For accurate surface energies, highly converged bulk energies are required, since the total energy of six bulk units is subtracted from that of the slab (i.e. three bulk units per surface). Therefore, the Alavi-Spencer scheme<sup>121</sup> was used to correct the Coulomb divergence (`HFRCUT=-1` in VASP) during bulk calculations.

### 1.3 LC-srPBEx25 Functional

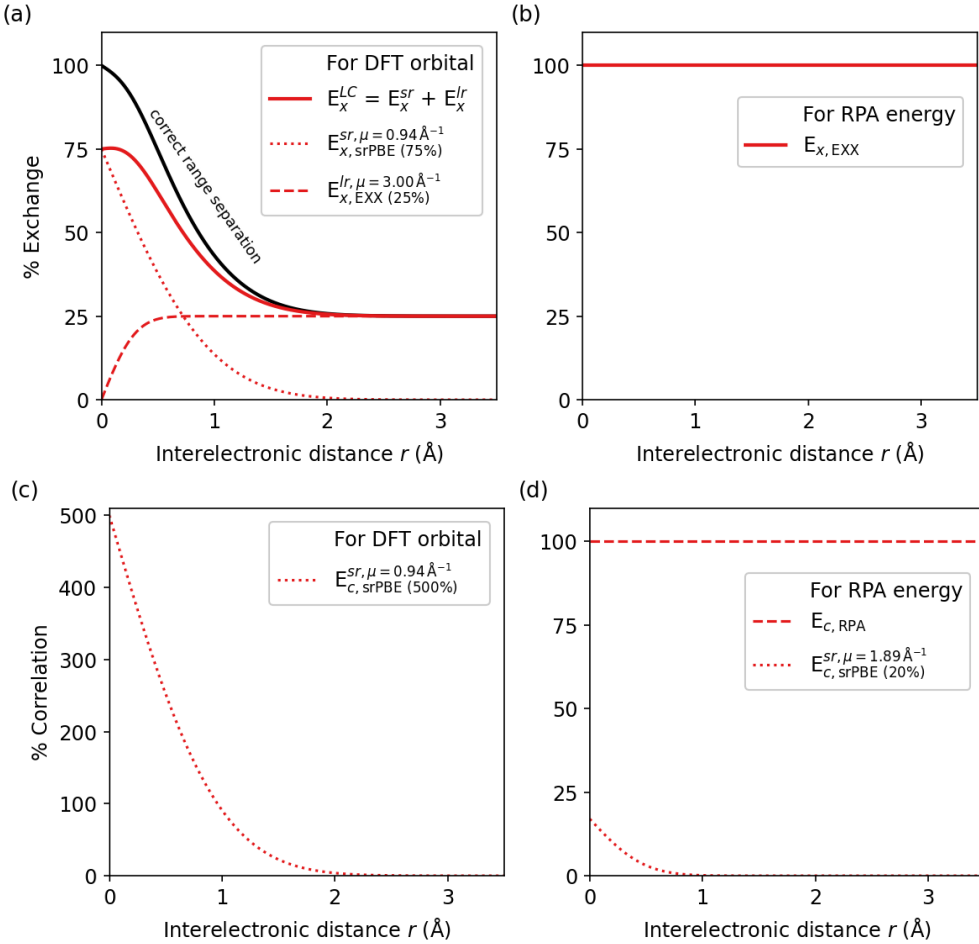


Figure S1: Range separation of exchange (a, b) and correlation (c, d) for LC-srPBEx25 functional (a, c) and the RPA energy evaluation (b, d). The incorrect range separation of exchange in LC-srPBEx25 (solid red line in (a)) is compensated by increasing the srPBE correlation to 500% (c). In (d), a small fraction of srPBE correlation is applied when evaluating the exchange part of RPA energy to reduce the scaling constant closer to 1.

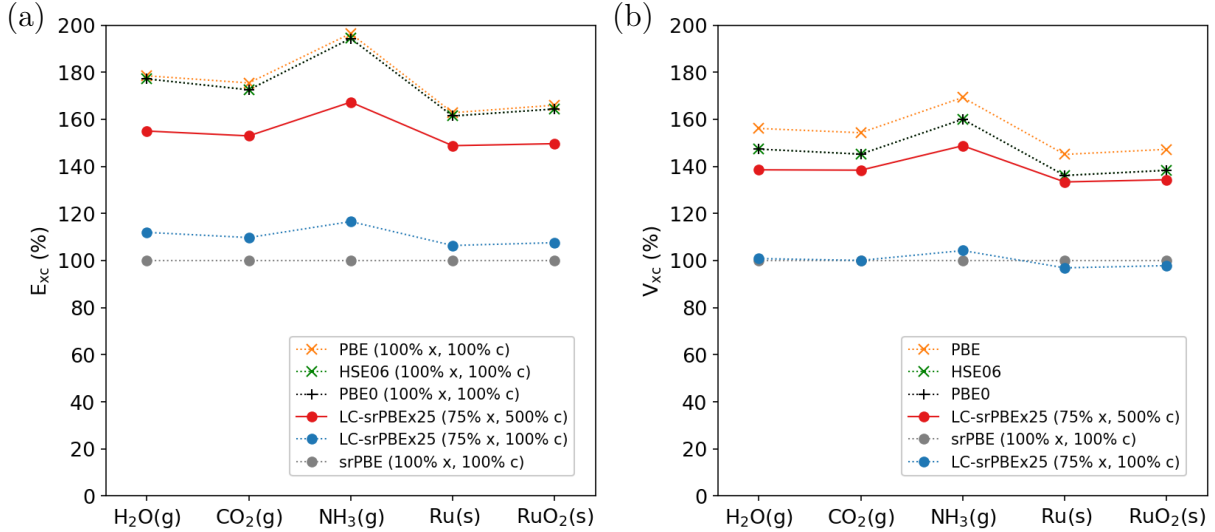


Figure S2: The xc energy (a) and the expectation value of xc potential (b), shown relative to srPBE with 100% exchange and 100% correlation, for different functionals. EXX contributions are included. Increasing the correlation contribution in LC-srPBEx25 compensates for the underestimated exchange contributions.

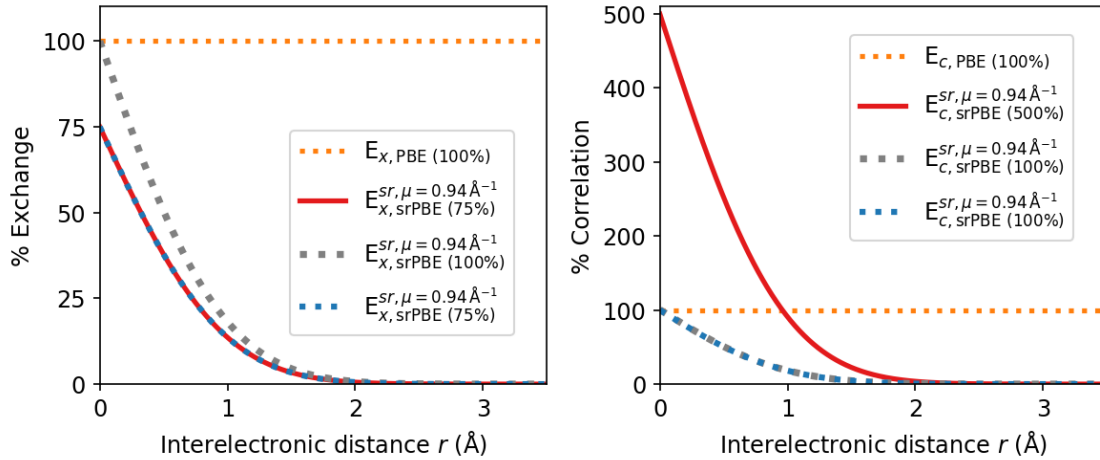


Figure S3: Range separation of exchange (left) and correlation (right) for PBE and LC-srPBEx25 functionals with different amount of xc contributions. Colors correspond to Fig. S2.

Table S1: MAD (RMSD) of charge densities relative to HSE06 values ( $\times 10^{-4}$  Ry $^{-3}$ ).

Method	Si bulk	Si atom	H <sub>2</sub> O
HSE06+D3	0	0	0
PBE+D3	2.80 (4.55)	0.05 (0.35)	0.12 (1.44)
r2SCAN+rVV10	0.84 (1.43)	0.05 (0.36)	0.03 (0.48)
LC-srPBEx25	1.98 (3.41)	0.13 (0.60)	0.24 (4.91)

Table S2: H<sub>2</sub>O(g) formation energy (eV) evaluated using various combinations of functionals. Columns correspond to functionals used to obtain charge densities and orbitals, and rows to those used to evaluate the energies in a non-self-consistent manner. Diagonal values represent self-consistent results.

	HSE06+D3	PBE+D3	r2SCAN+rVV10	LC-srPBEx25
HSE06+D3	-2.638	-2.642	-2.642	-2.679
PBE+D3	-2.516	-2.512	-2.518	-2.531
r2SCAN+rVV10	-2.495	-2.497	-2.491	-2.551
LC-srPBEx25	-3.761	-3.735	-3.782	-3.718

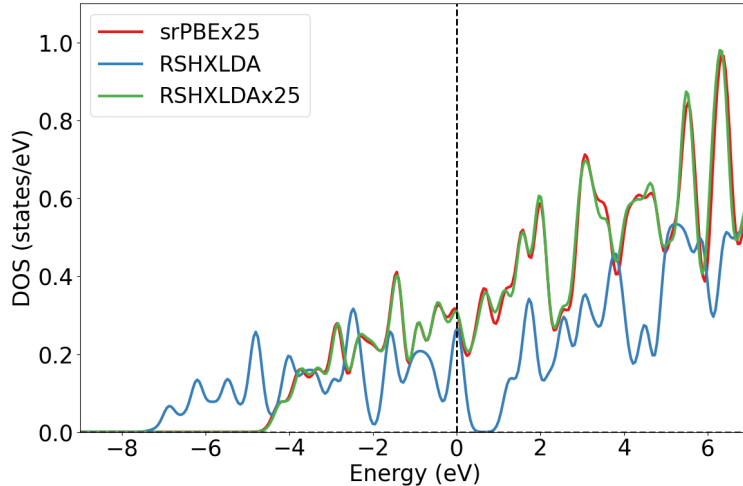


Figure S4: Density of states of bulk Na calculated using different functionals. LC-srPBEx25 retains states near the Fermi level, unlike RSHXLDA with 100% long-range EXX.

## 1.4 Energy Convergence

### 1.4.1 Metal bulk and surface

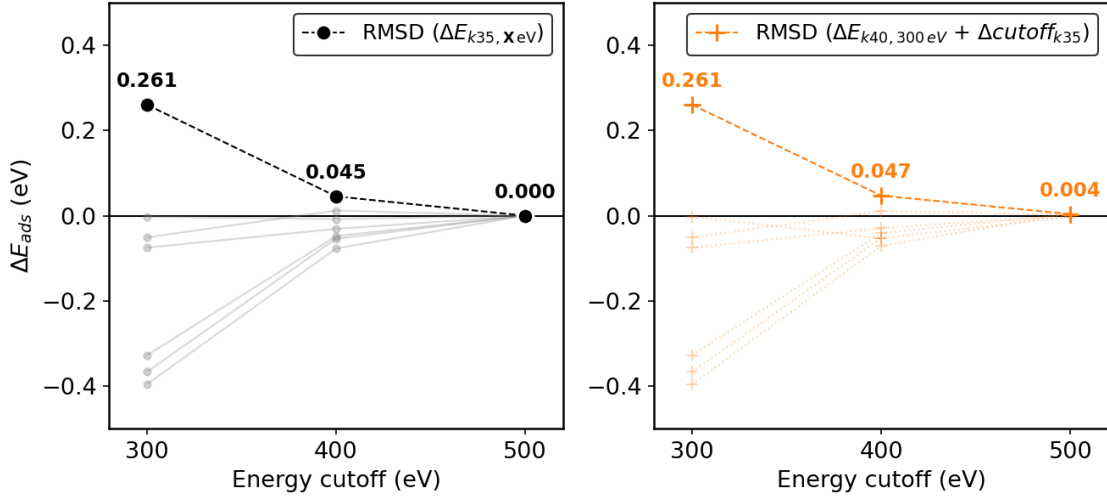


Figure S5: (Left) Convergence of adsorption energy on metal surfaces with respect to  $E_{cutoff}$  at  $k_{35}$  mesh, referenced to  $\Delta E_{k35, 500}$ . (Right) Validation of the correction term  $\Delta cutoff$  at different  $E_{cutoff}$ , referenced to  $\Delta E_{k40, 500}$ . The  $\Delta cutoff$ -corrected  $\Delta E_{k40, 300}$  values closely match  $\Delta E_{k40, 500}$ , demonstrating the effectiveness of the correction. Semi-transparent symbols correspond to individual values, while opaque symbols indicate RMSDs relative to the references.

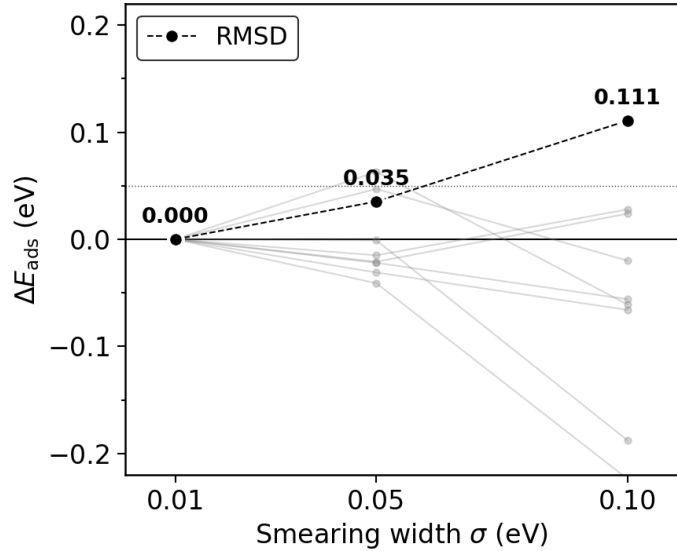


Figure S6: Convergence of adsorption energy on metal surfaces with respect to smearing width, referenced to values obtained with  $\sigma=0.01$  eV. Semi-transparent symbols correspond to individual values, while opaque symbols indicate RMSDs relative to the reference.

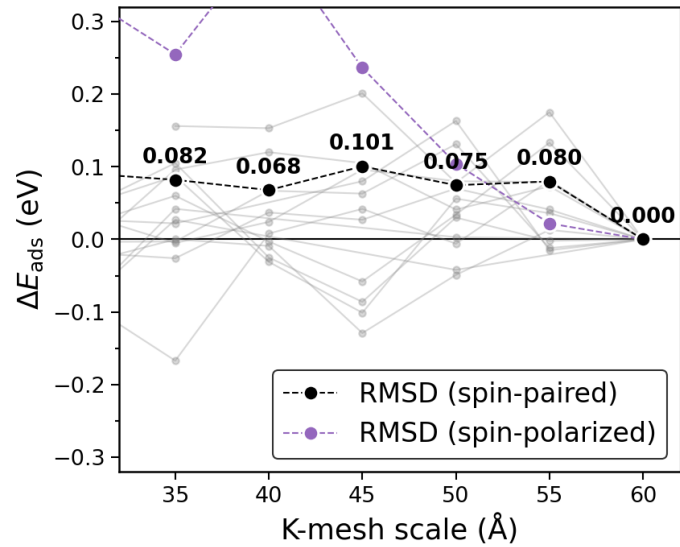


Figure S7: Convergence of adsorption energy on metal surfaces with respect to k-mesh scale, referenced to  $\Delta E^{k60}$ . Semi-transparent symbols correspond to individual values, while opaque symbols indicate RMSDs relative to the references. Black symbols correspond to spin-paired results of non-magnetic systems, and purple symbols correspond to spin-polarized results of Ni(111) systems.

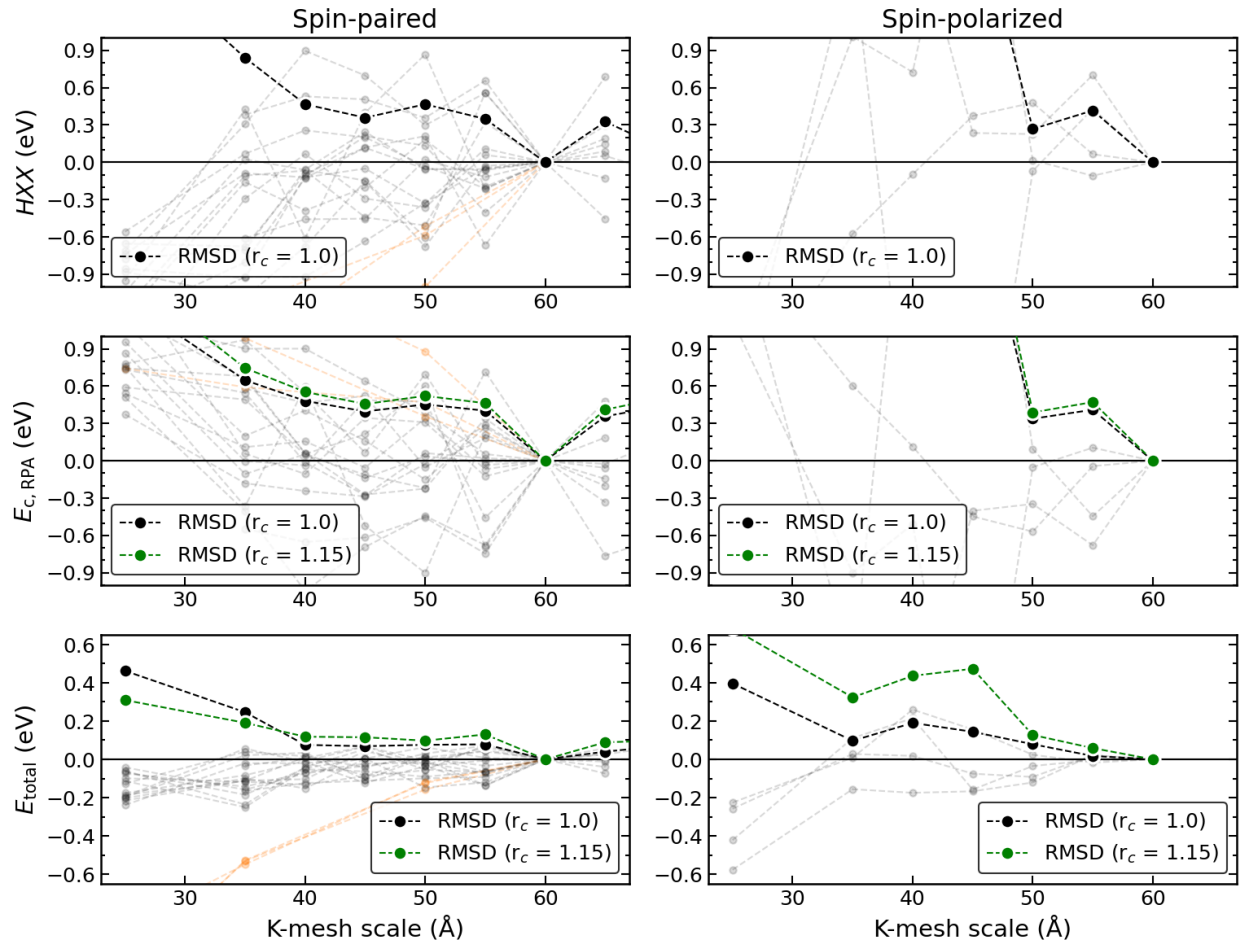


Figure S8: Convergence of HXX (top), RPA correlation energy (middle), and total energy ( $= \text{HXX} + E_{c,\text{RPA}}$ ) (bottom) of metal surface systems with respect to k-mesh scale, referenced to k60 values ( $r_c=1.0$  or  $r_c=1.15$ ). The left panels correspond to spin-paired results of non-magnetic systems, and the right panels correspond to spin-polarized results of Ni(111) systems. Semi-transparent symbols correspond to individual values ( $r_c=1.0$ ), while opaque symbols indicate RMSDs relative to the references. Orange symbols correspond to  $3 \times 3$  slabs ( $r_c=1.0$ ). Increasing the scaling factor from 1.0 to 1.15 worsens energy convergence.

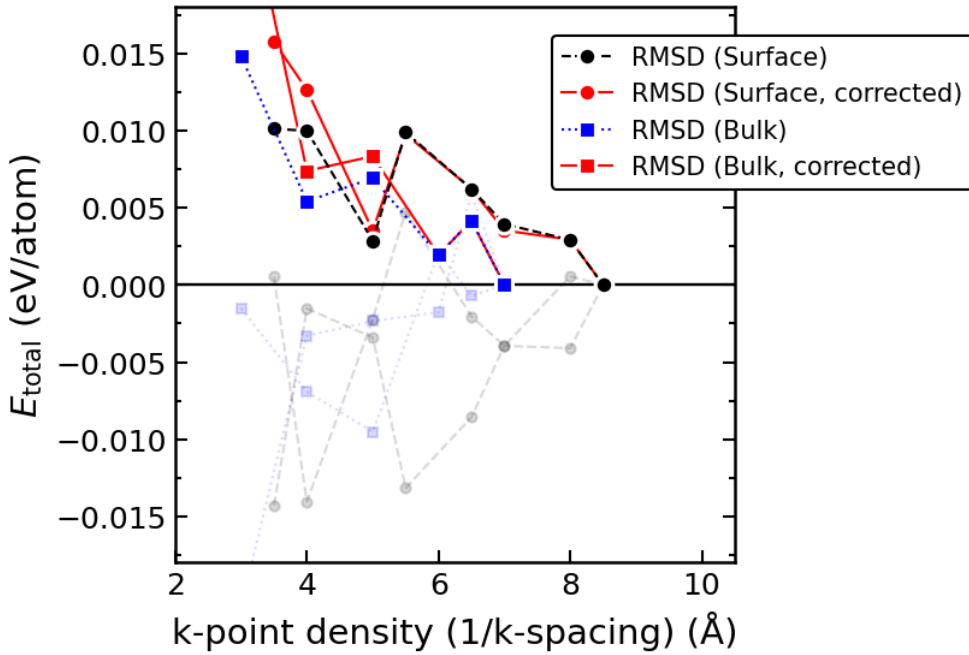


Figure S9: Convergence of total energy ( $= \text{HXX} + E_{c,\text{RPA}}$ ) of bulk and surface systems of Pd and Pt with respect to k-mesh scale, referenced to k-point densities of 7 Å (bulk) and 8.5 Å (= k65) (surface) ( $r_c=1.02$ ). Semi-transparent symbols correspond to individual values, while opaque symbols indicate RMSDs relative to the references. Red symbols correspond to results with a correction to the non-RPA correlation part for partial occupancies (ACFDT corr. in VASP). The present work does not include this correction term.

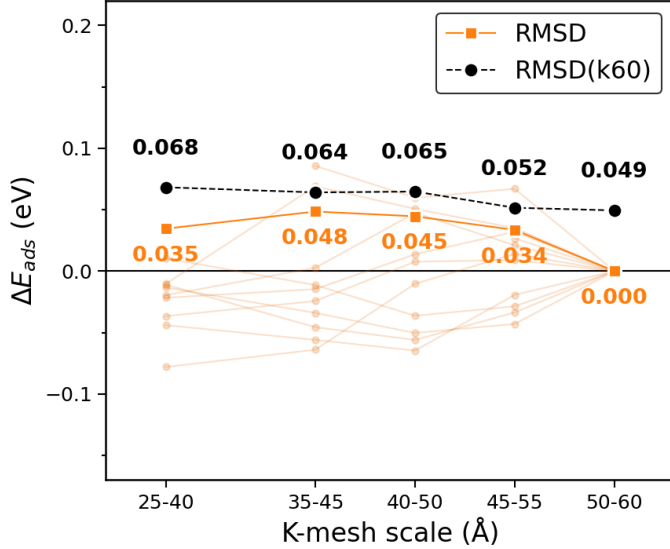


Figure S10: Convergence of averaged adsorption energy on metal surfaces with respect to k-mesh scales. Each y-axis value represents the averaged adsorption energy over three consecutive k-mesh scales (e.g., “25–40” values are averaged over k25, k35, and k40). The values are referenced to the averaged k50–k60 values (orange) or individual k60 values (black). Semi-transparent symbols correspond to individual values, while opaque symbols indicate RMSDs relative to the references.

#### 1.4.2 Oxide surface

For the MgO surface, a  $3 \times 3$  supercell with 2 layers was used for the baseline calculations. A  $3 \times 3$  supercell with four layers (4L) was used to obtain the correction for surface thickness ( $\Delta_{layer}$ ). A  $5 \times 5$  supercell with two layers (2L) was used to obtain the correction for supercell size ( $\Delta_{supercell}$ ).

$$\Delta_{layer} = \Delta E_{k15, 400, 4L} - \Delta E_{k15, 400, 2L}$$

$$\Delta_{supercell} = \Delta E_{k15, 400, 5 \times 5} - \Delta E_{k15, 400, 3 \times 3}$$

$$\Delta E_{\text{high-k, high-E, 4L, } 5 \times 5} \approx (\Delta E_{\text{high-k, low-E}} + \Delta_{\text{cutoff}}) + \Delta_{layer} + \Delta_{supercell}$$

The calculations for the  $\text{Al}_2\text{O}_3$  surface used a  $2 \times 2$  supercell with 12 layers, without corrections for slab thickness or supercell size. For the  $\text{TiO}_2$  surface, a  $1 \times 3$  supercell with 6 layers (6L) was used for the baseline calculations, and a  $1 \times 3$  supercell with 7 layers (7L) was used

to obtain the correction for surface thickness ( $\Delta_{\text{layer}}$ ).

$$\Delta_{\text{layer}} = \Delta E_{\text{k1}, 600, 7L} - \Delta E_{\text{k1}, 600, 6L}$$

$$\Delta E_{\text{high-k, high-E, 7L}} \approx (\Delta E_{\text{high-k, low-E}} + \Delta_{\text{cutoff}}) + \Delta_{\text{layer}}$$

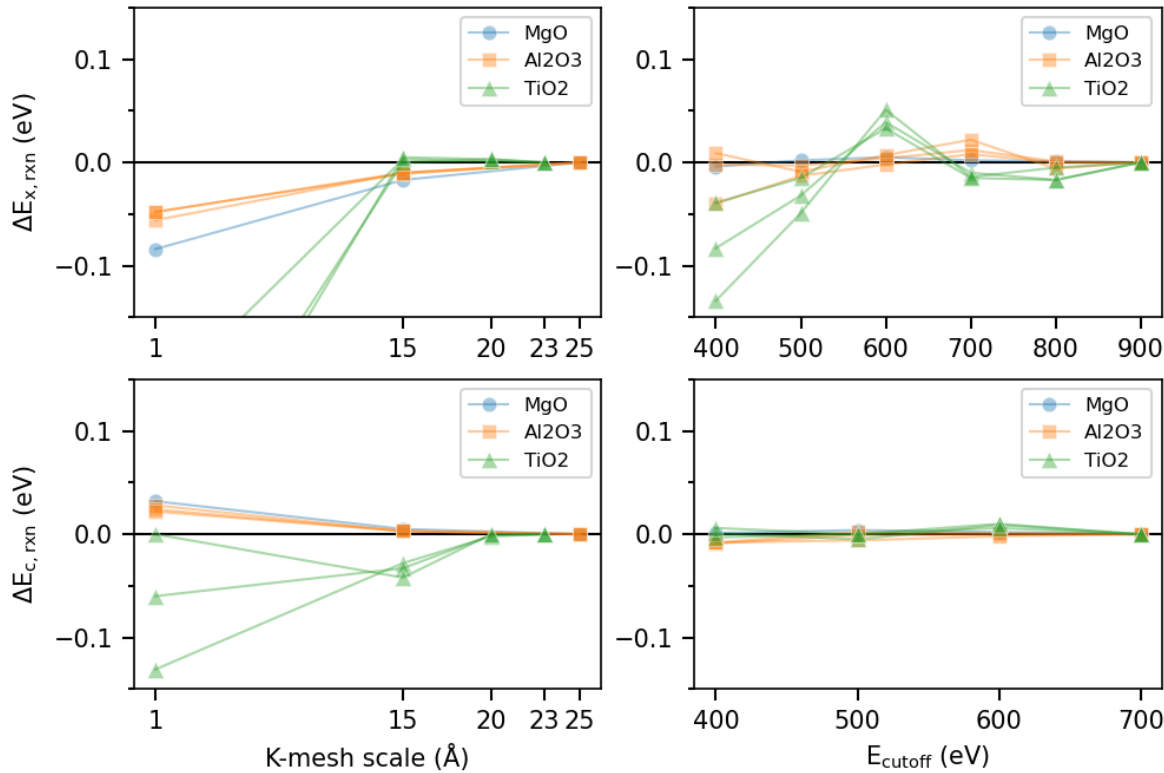


Figure S11: Convergence of surface reaction energy on the oxide surfaces. The top and bottom panels show the non-RPA correlation and RPA correlation contributions, respectively. Results are plotted with respect to k-mesh scale (left) and  $E_{\text{cutoff}}$  (right).

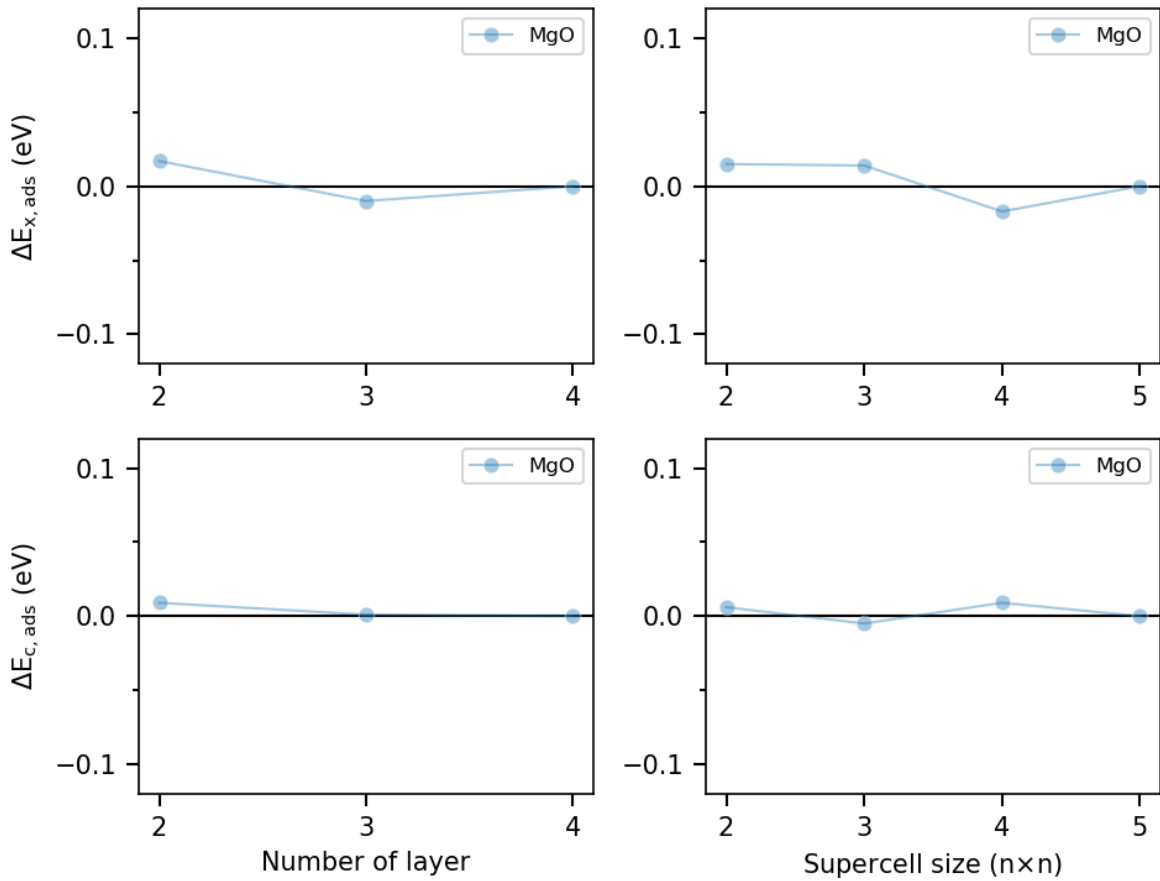


Figure S12: Convergence of adsorption energy on the MgO surface. The top and bottom panels show the non-RPA correlation and RPA correlation contributions, respectively. Results are plotted with respect to the number of surface layers (left) and the supercell size (right). A k-mesh scale of 15 Å was used. The surface structures have a supercell size of 3×3 (left) and consist of two layers (right).

### 1.4.3 Energy of infinitely dilute gas

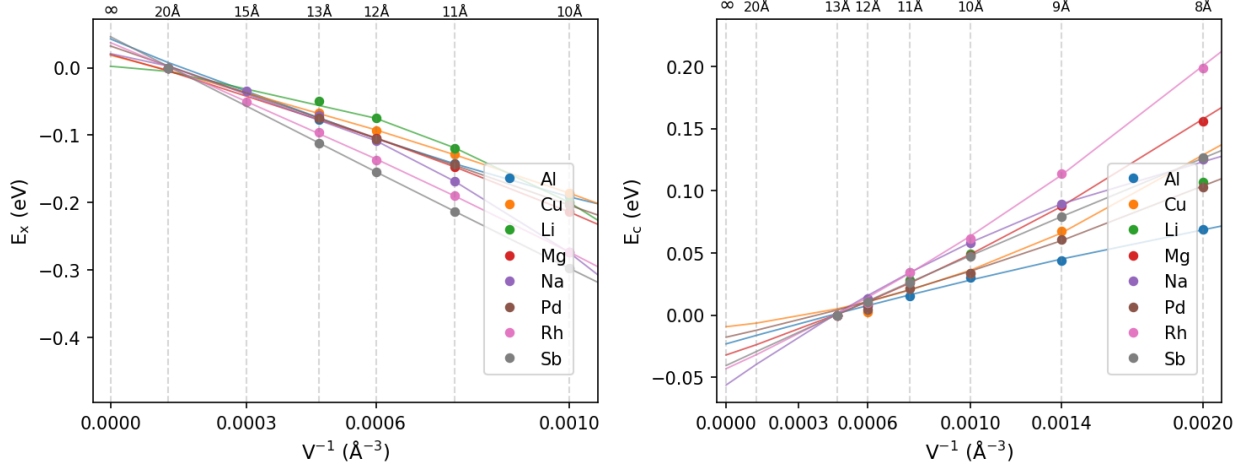


Figure S13: Volume dependence of  $E_{\text{HXX}}$  (a) and  $E_{\text{c,RPA}}$  (b) of gas species used for bulk properties, referenced to the energies at cell lengths of 20Å and 13Å, respectively. The solid lines represent the extrapolated energies using values at 10 – 13Å ( $E_x$ ) or 8 – 11Å ( $E_c$ ) cubic cells.

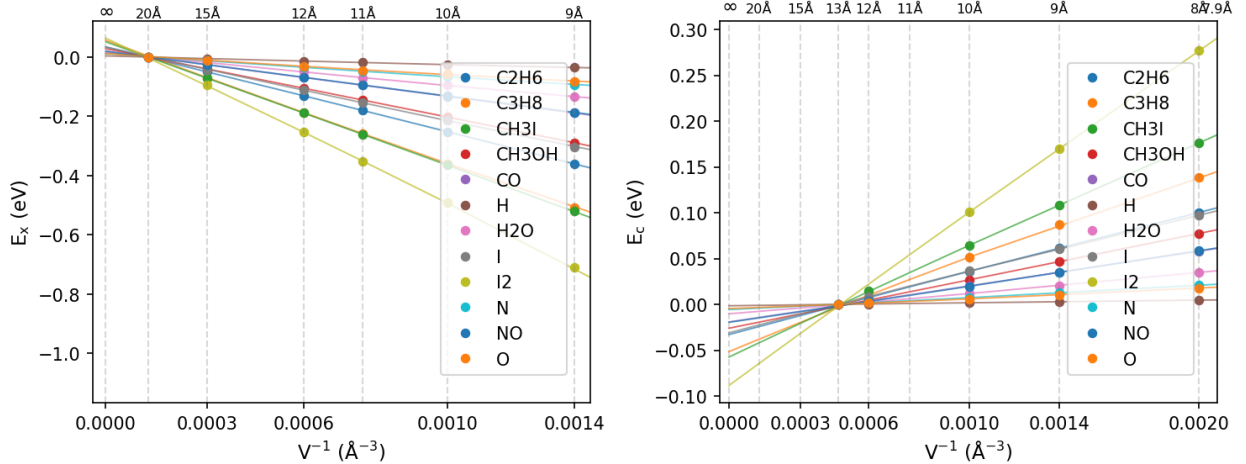


Figure S14: Volume dependence of  $E_{\text{HXX}}$  (a) and  $E_{\text{c,RPA}}$  (b) of adsorbates, referenced to the energies at cell lengths of 20Å and 13Å, respectively. The solid lines represent the extrapolated energies using values at 8 – 11Å ( $E_x$ ) or 8 – 10Å ( $E_c$ ) cubic cells.

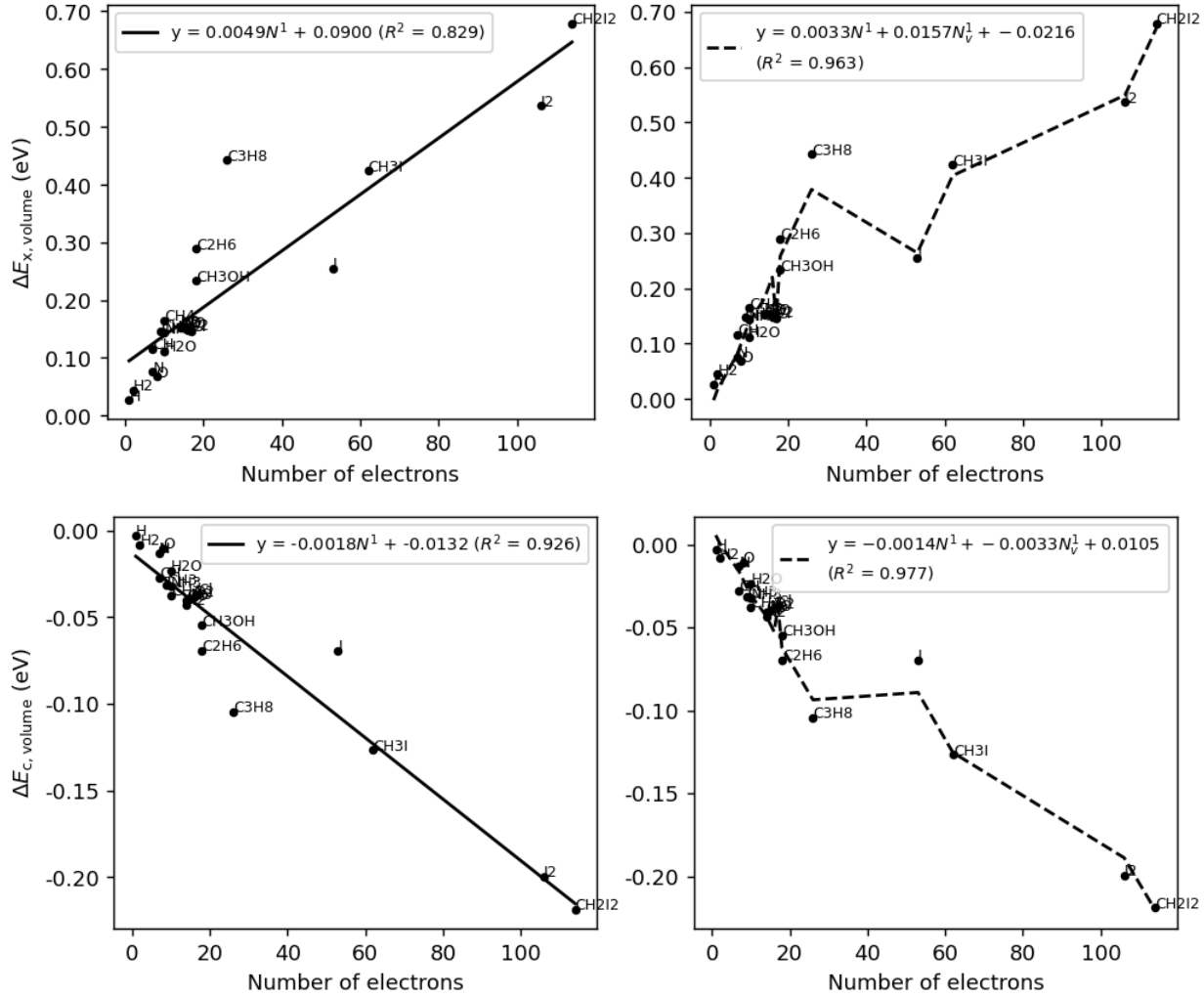


Figure S15:  $\Delta E_{\text{volume}}$  ( $= E_{\infty} - E_{10\text{\AA}}$ ) at optRPA26 level as a function of the total number of electrons ( $N$ ) in gas-phase species. Top panels show the exchange contribution  $\Delta E_{\text{x,volume}}$ , and bottom panels show the correlation contribution  $\Delta E_{\text{c,volume}}$ . Left panels include linear fits in  $N$ , while right panels include fits as functions of  $N$  and  $N_{\text{v}}$  (number of valence electrons).

## 1.5 Notes for RPA calculations

To reduce the cost of SCF cycles, the q-point grid can be reduced (NKRED-related tags) to pre-converge the wavefunction. In the next step, the calculation of unoccupied bands takes 500–2000 cpu hours, but only a single non-SCF step (one iteration) is required to determine the unoccupied bands. In the low-scaling RPA routine in VASP, the calculation of unoccupied bands is done internally, but this can be avoided by manually setting the number of bands.

Separating the calculation of unoccupied bands allows the use of parallelization settings that are not available during the RPA routine. The actual evaluation of RPA correlation energy only takes  $\sim$ 500 cpu hours, but this step requires memory of 4000–6000 GB (which can be reduced by  $\sim$ 1.5 by lowering NTAUPAR tag to adjust parallelization of imaginary time calculation). The large memory requirement can be handled by adjusting the number of CPUs allocated per task (via `--cpus-per-task` option in the Slurm workload manager), i.e., by using more nodes and less CPUs per node.

## 1.6 Miscellaneous

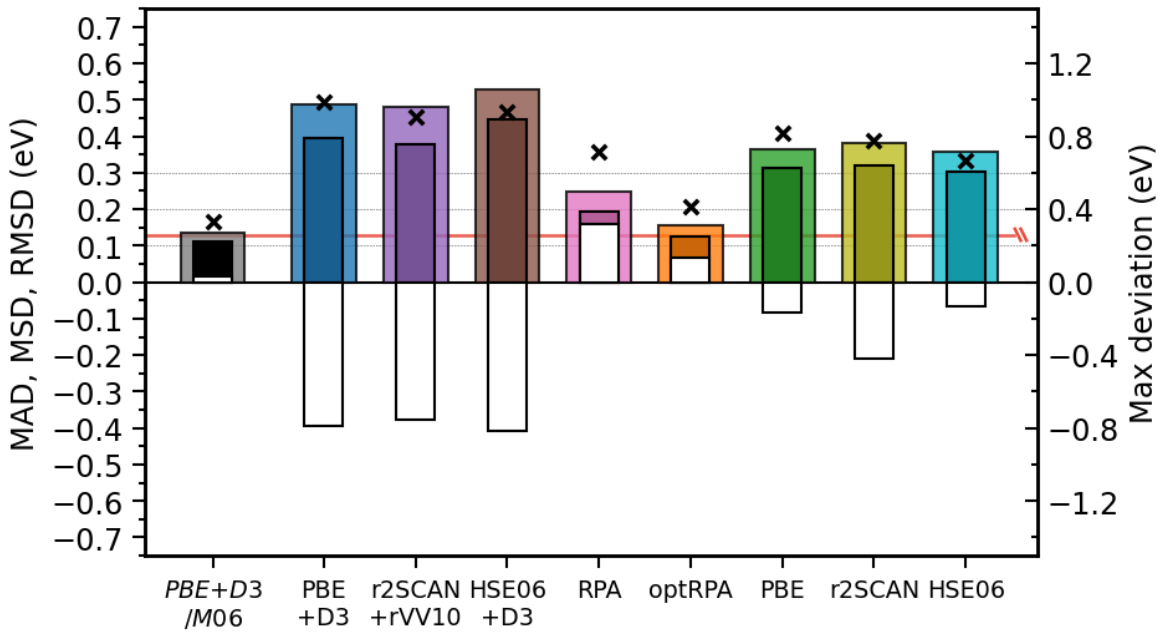


Figure S16: Deviations from ZPE-corrected experimental adsorption energies<sup>40</sup> on metals (Cu, Ru, Rh, Pd, Ir, Pt, and Ni) (n=27).  $PBE+D3/M06^{40}$  refers to a hybrid scheme that combines cluster (M06 level) and periodic model (PBE+D3 level). Non-dissociative adsorption energies referenced to gas-phase adsorbates (e.g., O) as in Ref. 40. The adsorption energy values are defined on a per-adsorbate basis; for example, for O adsorption, the adsorption energy is  $\Delta E$  in (a, c) or  $\Delta E/2$  in (b). Bars represent MAD (dark color), MSD (white color), and RMSD (light color), and  $\times$  symbols indicate maximum deviations. Red horizontal lines denotes the transition metal chemical accuracy of 3 kcal/mol.

Table S3: RMSDs of least-squares energies obtained from slab-based adsorption energies ( $E_{\text{slab+ads}} - E_{\text{slab}}$ ) and gas-phase adsorbate energies ( $E_{\text{ads(g)}}$ ) to separate errors originating from slabs and gas-phase adsorbates. For  $E_{\text{ads(g)}}$ , each adsorbate is included multiple times based on its occurrence in the adsorption dataset (e.g., O adsorbate is used three times).

$E_i$ (in Eq. (11))	<b>PBE+D3/M06</b>	<b>PBE</b> +D3	<b>r2SCAN</b> +rVV10	<b>HSE06</b> +D3	<b>RPA</b>	<b>optRPA26</b>
$E_{\text{slab+ads}} - E_{\text{slab}}$	0.119	0.175	0.175	0.277	0.172	0.108
$E_{\text{ads(g)}}$	0.051	0.172	0.139	0.135	0.115	0.050

$E_i$ (in Eq. (11))	<b>PBE</b>	<b>r2SCAN</b>	<b>HSE06</b>
$E_{\text{slab+ads}} - E_{\text{slab}}$	0.175	0.170	0.267
$E_{\text{ads(g)}}$	0.164	0.126	0.127

# TOC Graphic

